Desalination 639 (2026) 120683

Contents lists available at ScienceDirect

Desalination

journal homepage: www.elsevier.com/locate/desal

Contactless evaporation for solar desalination: A review of fundamental principles and innovative designs

Zhiheng Qiu [a], Xin Wei [a], Yinghao Song [a], Nan Deng [a], Ronghui Qi [b], Omar AlAli [c],*, Mengying Li [a],*

[a] Department of Mechanical Engineering & Research Institute for Smart Energy, The Hong Kong Polytechnic University, Hong Kong Special Administrative Region
[b] School of Chemistry and Chemical Engineering, South China University of Technology, Guangzhou, China
[c] Department of Mechanical Engineering, College of Engineering and Petroleum, Kuwait University, Kuwait

HIGHLIGHTS

- Outlines key physical mechanisms and multiphysics modeling for contactless evaporation.
- Analyzes evaporator material trends and key challenges in geometric design optimization.
- Identifies critical gaps in designing integrated salt–freshwater co-production systems.
- Proposes four prioritized directions for future research in the field.

ARTICLE INFO

Keywords:
Solar desalination
Contactless evaporation
Photothermal materials
Device designs
Research gaps and directions

ABSTRACT

Solar-driven interfacial evaporation is widely considered a promising low-cost and sustainable technology for desalination; yet, persistent salt fouling on photothermal layers severely limits its long-term stability under high-salinity conditions. Contactless evaporation provides an alternative strategy by physically separating the photothermal absorber from saline water with an air gap, where longwave infrared radiation serves as the dominant heat transfer pathway to drive interfacial evaporation. This design fundamentally prevents direct salt deposition on photothermal components and offers a promising route toward stable solar desalination in harsh brine environments. Although contactless evaporation has developed rapidly since its introduction in 2018, it has rarely been reviewed as an independent research field. This review presents a focused overview of contactless evaporation for solar desalination. The coupled transport mechanisms of radiative, conductive, and convective heat transfer, together with vapor diffusion across the air gap, are first summarized. Then, modeling approaches ranging from one-dimensional thermal resistance networks to two- and three-dimensional finite-element multiphysics simulations are outlined. Recent advances are then categorized into three major directions: spectrally matched absorber-emitter materials, geometric optimization of parallel and non-parallel architectures to balance radiative coupling and vapor transport, and hybrid systems integrating contactless and conventional interfacial evaporation for heat loss suppression and residual heat recovery. Representative devices are further compared in terms of evaporation performance, anti-scaling durability, scalability, and economic potential. Finally, key challenges are identified, including insufficient multiphysics modeling under realistic conditions, limited spectral co-design of materials, structural trade-offs between heat delivery and vapor escape, and the lack of standardized desalination-oriented evaluation metrics. Future efforts should focus on unified high-fidelity modeling, spectral engineering, integrated geometric and heat-recovery design, and standardized performance reporting.

Contents

* Corresponding authors.
E-mail addresses: o.alali@ku.edu.kw (O. AlAli), mengying.li@polyu.edu.hk (M. Li).

https://doi.org/10.1016/j.desal.2026.120683
Received 17 June 2026; Received in revised form 28 July 2026; Accepted 15 August 2026
Available online 22 August 2026

1. Introduction

The Earth's freshwater resources represent less than 3% of the total water volume [1]. Many regions are facing a serious shortage of freshwater due to geographical or climatic conditions, a situation that greatly restricts local economic and social development [2]. Desalination of seawater or brackish water has emerged as a critical solution to address this freshwater scarcity [3]. However, mainstream desalination technologies like reverse osmosis (RO) and conventional thermal desalination (such as multi-stage flash distillation (MSF) and multi-effect distillation (MED)) are energy-intensive and heavily reliant on fossil fuels [4], leading to high operational costs and carbon emissions. This creates a particular challenge for remote, arid regions that ironically have abundant solar resources but lack robust energy infrastructure [5]. Therefore, developing solar-driven desalination technologies represents a crucial pathway for sustainable freshwater production [6].

Solar interfacial evaporation represents a promising advancement in solar desalination. Unlike conventional methods that waste energy through multiple conversion steps, such as indirect systems (photovoltaic-powered RO, solar-driven MED [7] and solar-driven MSF [8]) or direct systems (solar stills [9] and solar membrane distillation [10]), solar interfacial evaporation converts solar energy into localized heat exactly at the water surface, generating vapor exclusively at the gas–liquid interface [11]. By bypassing these inefficiencies and confining heat strictly to the evaporation zone, solar interfacial evaporation significantly improves overall efficiency while reducing system complexity. Consequently, it has attracted widespread attention for its potential to enable low-cost, sustainable desalination and has driven innovative materials and system designs that maximize evaporation area and improve heat localization, including 3D-structured evaporators, bionic evaporators, and suspended evaporators (Fig. 1a). However, despite these advances, solar interfacial evaporation still faces limitations due to salt fouling. Since the photothermal layer is in contact with seawater, salt crystals inevitably deposit on the absorber surface, reducing light absorption, blocking water transport channels, and compromising overall system efficiency and stability over time [12,13]. While current mitigation strategies attempt to redirect salt accumulation by enhancing salt back-diffusion through Marangoni flow [14], accelerating water replenishment [15], and introducing self-cleaning structures [16], this only delays the problem; during extended operation, the salts eventually spread back onto the active surface and cause performance degradation.

Physically separating the solar photothermal absorber from the brine surface represents the optimal strategy to fully suppress salt fouling. Suspending the absorber above water creates an intrinsic air barrier that blocks salt crystal deposition; however, this intervening air gap disrupts conductive heat transfer to bulk water and may compromise evaporation performance. This thermodynamic limitation has been resolved via a tri-layer suspended photothermal architecture that couples solar light absorption and thermal radiative emission, a configuration formally termed "contactless evaporation" (Fig. 1b). For unambiguous terminology, we adopt the strict original definition proposed by Cooper et al. [20]: "contactless evaporation" denotes a solar

Nomenclature

Latin symbols

A	Surface area, m^2
A_{abs}	Absorber surface area, m^2
A_{emt}	Emitter surface area, m^2
A_w	Water surface (evaporation) area, m^2
A_i	Area of surface i ($i = 1, 2, 3$), m^2
C	Molar concentration of water vapor, mol/m^3
$C_{sat,w}$	Saturated vapor concentration at water surface, mol/m^3
C_∞	Ambient vapor concentration, mol/m^3
D_{wa}	Mass diffusivity of water vapor in air, m^2/s
E_{bi}	Blackbody emissive power of surface i, W/m^2
F_{ij}	View factor from surface i to surface j
g	Gravitational acceleration, m/s^2
G_{sun}	Solar irradiance, W/m^2
h	Convective heat transfer coefficient, $W/(m^2\ K)$
h_{abs}	Convective heat transfer coefficient at absorber, $W/(m^2\ K)$
h_w	Convective heat transfer coefficient at water surface, $W/(m^2\ K)$
h_{emt}	Convective heat transfer coefficient at emitter, $W/(m^2\ K)$
h_m	Convective mass transfer coefficient, m/s
h_{fg}	Latent heat of vaporization of water, J/kg
J_i	Radiosity of surface i, W/m^2
k_{air}	Thermal conductivity of air, $W/(m\ K)$
k_{water}	Thermal conductivity of water, $W/(m\ K)$
k_{sub}	Thermal conductivity of substrate, $W/(m\ K)$
L_c	Characteristic length, m
L_{sub}	Substrate thickness, m
d	Air gap thickness, m
$\dot{m}$	Evaporation mass flow rate, kg/s
M_{H_2O}	Molar mass of water, kg/mol
Nu	Nusselt number
Nu_{emt}	Nusselt number for emitter
Nu_w	Nusselt number for water surface
Pr	Prandtl number
P_{vapor}	Partial pressure of water vapor, Pa

Latin symbols (continued)

q_{sun}	Absorbed solar power, W
$q_{abs,conv}$	Convective heat loss from absorber, W
$q_{abs,rad}$	Radiative heat loss from absorber, W
$q_{abs,cond}$	Conductive heat transfer from absorber to emitter, W
$q_{emt,out}$	Total heat leaving emitter, W
$q_{emt,conv}$	Convective heat transfer from emitter, W
$q_{emt,cond}$	Conductive heat transfer across air gap, W
$q_{emt,rad}$	Net radiative flux leaving emitter, W
$q_{w,rad}$	Radiative heat absorbed by water surface, W
$q_{w,in}$	Total heat arriving at water surface, W
$q_{w,conv}$	Convective heat loss from water surface, W
$q_{cond,loss}$	Conductive heat loss to bulk water, W
q_{evp}	Latent heat consumption for evaporation, W
R	Universal gas constant, $8.314\ J/(mol\ K)$
Ra	Thermal Rayleigh number
Ra_m	Mass transfer Rayleigh number
Re	Reynolds number
Sc	Schmidt number
Sh	Sherwood number
T_{abs}	Absorber temperature, K
T_{emt}	Emitter temperature, K
T_w	Water surface temperature, K
T_{bottom}	Bottom water temperature, K
T_a	Ambient temperature, K
T_{air}	Bulk air temperature in air gap, K
U_m	Mean wind speed, m/s
C_{emt}	Molar concentration of water vapor near the photothermal layer, mol/m^3
L_{water}	Thickness of water, m

Greek symbols

α_{abs}	Solar absorptance of absorber
ε_{abs}	Thermal emittance of absorber
ε_i	Thermal emittance of surface i
σ	Stefan–Boltzmann constant, $5.67 \times 10^{-8}\ W/(m^2\ K^4)$
α	Thermal diffusivity, m^2/s
ν	Kinematic viscosity of air, m^2/s
β_T	Thermal expansion coefficient, $1/K$
β_m	Concentration expansion coefficient, m^3/mol

desalination technique in which an air gap fully separates the photothermal layer from saline water, with longwave infrared radiation as the dominant heat transfer method to drive water evaporation. This definition fundamentally differentiates the technology from traditional interfacial evaporation systems, where photothermal materials are maintained in direct contact with the brine. Functionally, the trilayer structure captures incident solar irradiance via its top absorptive layer, while a tailored bottom emitter converts harvested thermal energy into downward-propagating infrared radiation. As illustrated in Fig. 2, the emitter operates at around 330 K, corresponding to a blackbody spectral emissive power peaked within the infrared band, where seawater possesses a high optical absorption coefficient that restricts radiation penetration to less than 1 cm. Nearly all longwave infrared flux is thus confined and absorbed at the air–water interface, realizing targeted interfacial heating for vapor generation.

Building upon the radiative heat transfer mechanism that distinguishes contactless evaporation from conventional interfacial evaporation, several recent reviews on solar-driven interfacial evaporation have touched upon this topic [22–25]. Like these earlier reviews, the present work is concerned with solar-driven evaporation/desalination systems enabled by photothermal conversion and thermal management. However, in the existing literature, contactless evaporation is typically confined to a single section or subsection, usually limited to a brief introduction of its working principle and representative

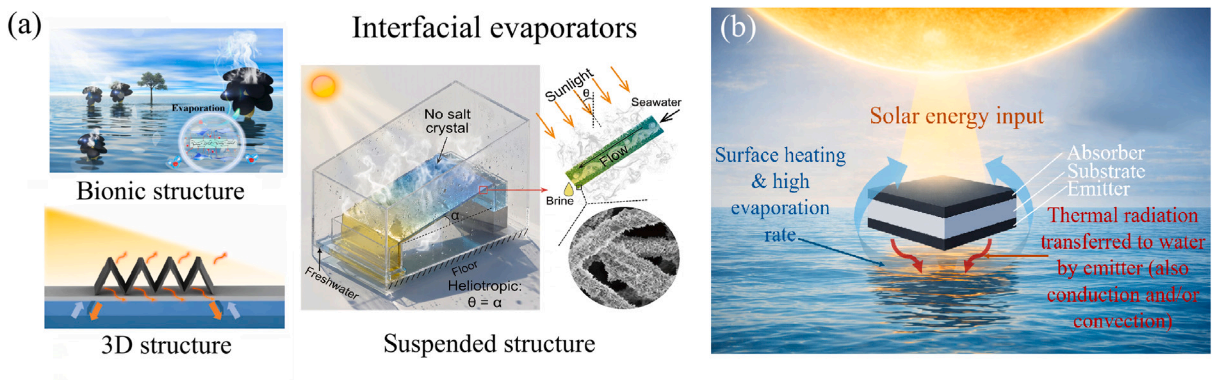

Fig. 1. (a) Innovative structural designs of solar interfacial evaporators, including a 3D structure [17], a bionic structure [18], and a suspended structure [19] (figures reproduced with permission). (b) Schematic diagram of a contactless evaporator and its operation principle, based on the concept presented in Cooper et al. [20].

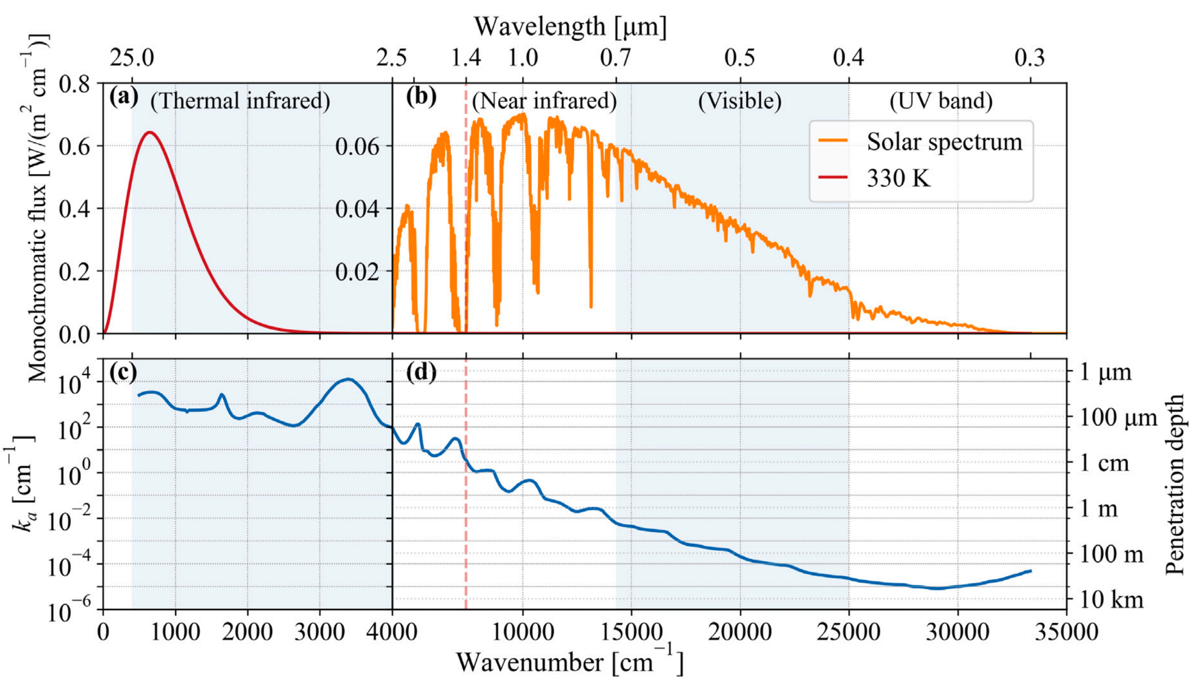

Fig. 2. Spectral radiance of sunlight and 330 K blackbody emissive power, as well as seawater absorption coefficients and penetration depths.
Source: Data adapted from Deng et al. [21].

schematic diagrams. As a result, contactless evaporation is generally treated either as a peripheral variant of interfacial evaporation or as a subordinate configuration related to air-gap distillation, rather than as an independent solar-desalination architecture with its own distinctive design logic and physical constraints. Consequently, its intrinsic energy transport pathways, radiative absorber–water coupling, vapor transport characteristics, and performance-limiting mechanisms have not yet been systematically discussed, as summarized in Table 1. This limited treatment is closely related to the field's development timeline. Following its conceptual introduction by Cooper et al. [20] in 2018, progress remained relatively incremental for several years, making a dedicated review premature. Since 2022, however, a growing body of rigorous studies has substantially advanced the understanding of photothermal materials, radiative coupling across air gaps, vapor transport dynamics, and structural optimization, resulting in a sufficiently cohesive knowledge base. To date, no dedicated review has synthesized these developments. A focused review is therefore both timely and necessary to consolidate the rapidly expanding literature, clarify the unique physical picture and design space of contactless evaporation, and identify the key challenges and opportunities for its practical implementation in solar desalination.

Despite its promise for suppressing salt fouling while enabling solar-driven desalination, contactless evaporation still faces several barriers to practical deployment. These include the difficulty of achieving efficient absorber–emitter spectral matching, vapor-transport resistance introduced by the air gap, convective heat loss from suspended heated structures, and the lack of standardized desalination-oriented performance evaluation. At the same time, recent progress in photothermal materials, geometric design, hybrid architectures, and application-oriented assessment has rapidly expanded the field, making the literature increasingly fragmented and difficult to compare on a common basis. To address this gap, this review provides a comprehensive and mechanism-oriented synthesis of contactless evaporation for solar desalination. It first examines the fundamental heat and mass transfer processes, as well as the associated multiphysics modeling approaches. It then reviews recent advances along three main innovation pathways: absorber and emitter materials, geometric and vapor transport optimization, and hybrid configurations that combine contactless and

Table 1
Systematic comparison of representative review articles and the scope of the present work.

Review	Shared ground with the present work	Distinct scope of the previous work	Why present work is needed
Bai et al. [23]	Solar-driven evaporation/desalination; practical performance issues	General interfacial evaporation with emphasis on reliable performance	Contactless evaporation is only briefly introduced, without dedicated mechanistic synthesis.
Wu et al. [25]	Water treatment/desalination; efficiency and scaling control	General solar-driven evaporators for water treatment	Contactless evaporation is treated mainly as one anti-scaling design.
Hou et al. [24]	Solar-driven interfacial evaporation performance evaluation and optimization	Broad Solar-driven interfacial evaporation review including materials, structures, and applications	Contactless evaporation remains a small subsection.
Song et al. [22]	Solar-driven evaporation for water-related applications	Food-energy-water nexus oriented, application-driven overview	Contactless evaporation is only briefly discussed in wastewater treatment/resource contexts.
Present work	Solar-driven desalination and evaporation	Dedicated contactless evaporation review	Focuses specifically on its unique radiative heat transfer pathway, detached evaporation geometry, and performance-limiting mechanisms.

interfacial evaporation. Beyond design innovation, this review also comparatively assesses current devices in terms of performance, durability, scalability, and cost characteristics, and critically summarizes the key limitations that still constrain field development. Based on this analysis, priority directions for future research are proposed, including mechanism-resolved modeling, spectrally informed material design, coupled geometric optimization, and standardized desalination-oriented evaluation centered on evaporation rate, freshwater productivity, and gained output ratio (GOR). This review aims to provide a clearer framework for understanding current progress and to support the transition of contactless evaporation from laboratory-scale demonstrations toward practically relevant solar desalination systems.

2. Fundamental principles of contactless evaporation

In contactless evaporation systems, energy transport and mass transfer are governed by coupled heat and fluid transport processes, including thermal radiation, conduction, natural/forced convection, and mass transport. These multiphysical processes lead to the complexity of coupled heat and mass transfer mechanisms. This section establishes a unified theoretical framework with governing equations and simplified engineering models, describing the internal coupling relationships of the four core mechanisms and providing a theoretical foundation for the design and performance evaluation of contactless evaporation systems.

2.1. Heat transfer of the photothermal layer

Existing contactless evaporation configurations primarily employ two vapor diffusion paradigms: one uses a channeled photothermal layer to facilitate vertical vapor escape, while the other incorporates lateral gaps to enable lateral vapor diffusion, as shown in Fig. 3a and b.

Regardless of the vapor-diffusion paradigm, the heat transfer mechanism follows the same pathway, as illustrated in Fig. 3c. Solar radiation is first absorbed by the top absorber and converted into thermal energy. This energy is then transferred by the emitter to the water surface and the surrounding environment through thermal radiation, as well as conduction and/or convection. Meanwhile, the absorber surface also undergoes parasitic heat losses to the ambient via convection and radiation. The corresponding energy balance is given by:

$$\begin{aligned} q_{\mathrm{sun}} &= q_{\mathrm{abs,conv}} + q_{\mathrm{abs,rad}} + q_{\mathrm{abs,cond}} \\ q_{\mathrm{abs,cond}} &= q_{\mathrm{emt,out}} = q_{\mathrm{emt,conv}} + q_{\mathrm{emt,cond}} + q_{\mathrm{emt,rad}} \end{aligned} \tag{1}$$

The absorption of solar energy, the heat losses of the absorber, and the heat transferred to the emitter can be evaluated as follows:

$$q_{\mathrm{sun}} = \alpha_{\mathrm{abs}} A_{\mathrm{abs}} G_{\mathrm{sun}} \tag{2}$$

$$q_{\mathrm{abs,conv}} = h_{\mathrm{abs}} A_{\mathrm{abs}} (T_{\mathrm{abs}} - T_a) \tag{3}$$

$$q_{\mathrm{abs,rad}} = \varepsilon_{\mathrm{abs}} \sigma A_{\mathrm{abs}} (T_{\mathrm{abs}}^4 - T_a^4) \tag{4}$$

$$q_{\mathrm{abs,cond}} = -k_{\mathrm{sub}} \frac{T_{\mathrm{abs}} - T_{\mathrm{emt}}}{L_{\mathrm{sub}}} \tag{5}$$

where α_{abs} is the absorptance of the absorber in the solar spectrum; A_{abs} [m^2] is the surface area of the absorber; G_{sun} [W/m^2] is the solar flux, where "one sun" corresponds to G_{sun} = 1000 W/m^2; h_{abs} [W/(m^2·K)] is the convective heat transfer coefficient, which mainly depends on wind speed; T_{abs} [K], T_{emt} [K], and T_a [K] are the absorber, emitter, and ambient temperatures, respectively; $\varepsilon_{\mathrm{abs}}$ is the emittance of the absorber in the thermal longwave spectrum; $\sigma = 5.67 \times 10^{-8}$ W/(m^2 K^4) is the Stefan–Boltzmann constant; k_{sub} [W/(m·K)] and L_{sub} [m] are the thermal conductivity and thickness of the substrate.

Energy is then dissipated from the emitter through radiation to the surroundings, the water surface, and by convection and conduction across the air gap. The calculation methods are presented in the following section.

2.2. Heat transfer across the air gap

2.2.1. Thermal radiation

The radiation emitted by the emitter will be partially absorbed by the water surface and partially absorbed by the environment or the sides of the device. The radiative heat transfer between the emitter, water surface, and surrounding boundaries can be considered as radiation exchange among three gray surfaces, as represented by the radiative resistance network (Fig. 3d). The corresponding radiosity and irradiation balances are [26]:

$$J_1 = \varepsilon_1 E_{b1} + (1 - \varepsilon_1)[J_1 F_{11} + J_2 F_{12} + J_3 F_{13}] \tag{6}$$

$$J_2 = \varepsilon_2 E_{b2} + (1 - \varepsilon_2)[J_1 F_{21} + J_2 F_{22} + J_3 F_{23}] \tag{7}$$

$$J_3 = \varepsilon_3 E_{b3} + (1 - \varepsilon_3)[J_1 F_{31} + J_2 F_{32} + J_3 F_{33}] \tag{8}$$

where "1" denotes the emitter surface, "2" denotes the water surface, and "3" denotes the surroundings; J_i [W/m^2] is the radiosity of the surface i; $E_{bi} = \sigma T_i^4$ [W/m^2] is the emissive power of surface i; ε_i is the emittance in the longwave spectrum of surface i; F_{ij} is the view factor from surface i to surface j. When all temperatures, emittance, and view factors are evaluated, the above equation set can be solved to obtain all radiosity values. Then, the net radiative flux leaving the emitter, as well as that being absorbed by the water surface, is,

$$q_{\mathrm{emt,rad}} = q_{1,\mathrm{net}} = \frac{E_{b1} - J_1}{(1 - \varepsilon_1)/\varepsilon_1 A_1} \tag{9}$$

$$q_{\mathrm{w,rad}} = q_{2,\mathrm{net}} = \frac{J_2 - E_{b2}}{(1 - \varepsilon_2)/\varepsilon_2 A_2} \tag{10}$$

where A_i [m^2] represents the surface area of i.

In some studies [27–29], the device geometry makes radiative exchange with the surrounding boundaries small enough to neglect (for example, with insulated side walls), so the emitter and water surface

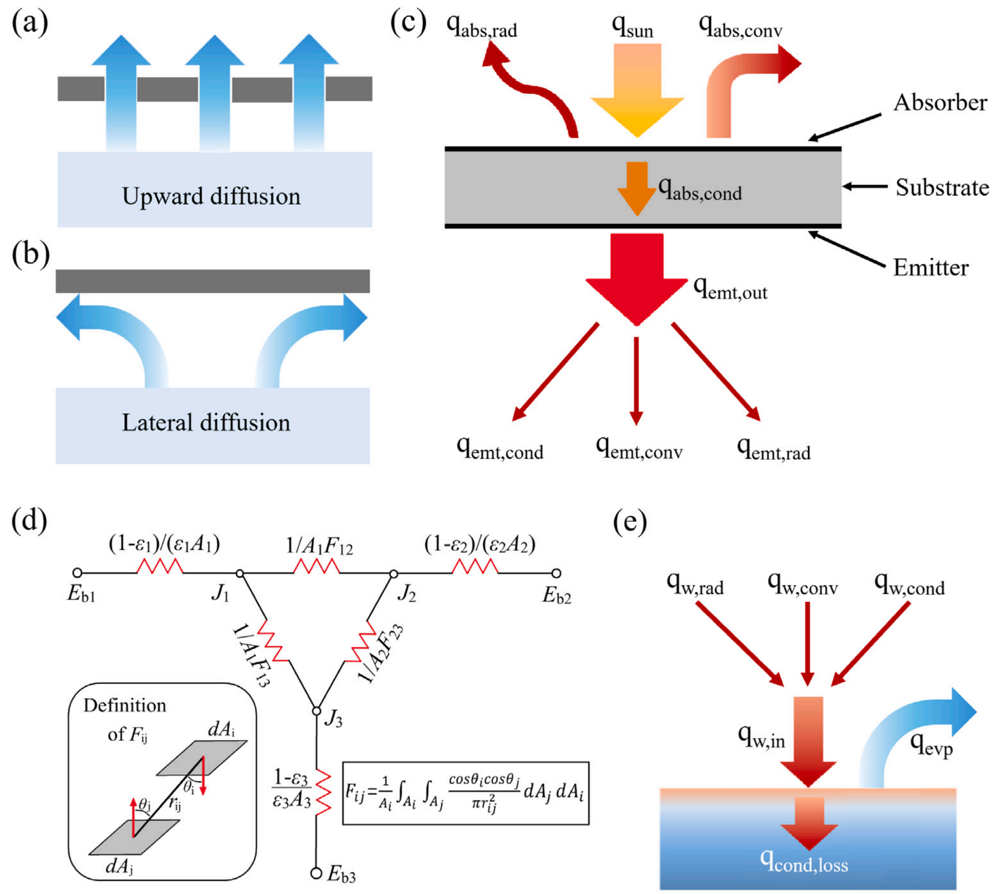

Fig. 3. Two vapor-diffusion paradigms around the photothermal layer: (a) upward diffusion and (b) lateral diffusion; (c) schematic of the photothermal layer's energy balance. (d) Radiative heat transfer network between the emitter (surface 1), the water surface (surface 2), and the surroundings (surface 3); both space resistances and surface resistances are expressed using surface areas, view factors and surface emittances. (e) Schematic diagram of the interfacial energy balance.

can be treated as two finite parallel planes. Under this assumption, the radiative heat transfer rate from the emitter to the water surface simplifies to:

$$q_{\mathrm{w,rad}} = \frac{\sigma\left(T_1^4 - T_2^4\right)}{\dfrac{1-\varepsilon_1}{\varepsilon_1 A_1} + \dfrac{1}{F_{12}A_1} + \dfrac{1-\varepsilon_2}{\varepsilon_2 A_2}} \quad (11)$$

where F_{12} is the view factor from the emitter to the water surface, which approaches unity when the plate separation is small relative to the plate dimensions. Achieving a high radiative flux, therefore, requires low radiative transfer resistance, which is determined by two design parameters: a high emitter emittance ε_1 and a geometry that maximizes the view factor F_{12} between the emitter and the water surface.

2.2.2. Heat conduction and natural convection

Although thermal radiation is generally regarded as the dominant heat transfer mechanism in contactless evaporation, it is not the sole contributor. Radiation operates over a distance without direct contact; therefore, an air gap inevitably remains between the emitter and the evaporating surface. Despite air having a relatively low thermal conductivity at ambient temperature [30], heat transfer across this gap via conduction or natural convection (in no wind conditions) still represents a non-negligible component of the overall energy transport.

As discussed in Section 2.1, contactless evaporators employ two primary vapor diffusion strategies: upward and lateral diffusion, each associated with distinct structural configurations. These designs significantly influence the relative importance of conductive and convective heat transfer within the air gap. For instance, under certain geometries, the air gap may be reasonably approximated as pure conduction, whereas in others, natural convection must be explicitly considered. In particular, lateral diffusion systems feature air gaps directly exposed to the ambient environment, raising critical questions: to what extent does heat convect from the emitter to the water surface, from the water surface to the surroundings, or even directly from the emitter to the ambient? Quantifying these contributions is therefore essential.

It is worth emphasizing that all reported studies on contactless evaporation to date have focused exclusively on natural convection; forced convection has not yet been introduced into such systems. Moreover, natural convection is physically more closely related to pure conduction than to turbulent or mixed convection regimes. Consequently, the discussion in this section is restricted to natural convection, providing a consistent and physically meaningful framework for analyzing heat transfer in contactless evaporation.

Conduction and natural convection in an upward diffusion system

The Rayleigh number (Ra) provides a quantitative criterion for determining whether heat transfer across the air gap should be treated as conduction or natural convection. Following the formulations adopted in recent upward diffusion system studies [20],

$$\mathrm{Ra} = \frac{g\beta_T (T_{\mathrm{emt}} - T_w) L_c^3}{\nu\alpha}, \quad \text{with } L_c = d \quad (12)$$

where $g = 9.81$ m/s^2 is the gravitational acceleration, β_T [1/K] is the thermal expansion coefficient, T_{emt} and T_w [K] are the temperatures of the emitter and the water surface, L_c [m] is the characteristic length of the water surface, ν [m^2/s] is the kinematic viscosity of air, α [m^2/s] is the thermal diffusivity of air, and d [m] is the thickness of the air gap.

Natural convection is expected to emerge once Ra exceeds a critical value of approximately 1708. Below this threshold, buoyancy-driven motion is suppressed, and heat transfer can be reasonably modeled as pure conduction.

In upward diffusion configurations, Ra values that have been reported [20] remains well below the critical limit. For other representative works [27–29], we took some estimates based on the data provided by these papers, also obtaining Ra values below the critical value. This behavior arises because the heated emitter is positioned above the cooler water surface, creating a stably stratified air layer that inhibits natural convection. Therefore, heat transfer should be modeled as purely heat conduction, which can be expressed as:

$$q_{\mathrm{emt,cond}} = \frac{k_{\mathrm{air}} A}{d} \left(T_{\mathrm{emt}} - T_w\right) \tag{13}$$

where k_{air} [W/(m K)] is the thermal conductivity of air, A [m^2] is the surface area of the emitter and the water surface.

The conductive thermal resistance decreases with diminishing d, making conduction increasingly dominant at sub-centimeter scales. For example, Zheng et al. [28] demonstrated that conductive heat transfer surpasses radiative transfer when $d < 4.3$ mm under $T_{\mathrm{emt}} = 80$ °C and $T_w = 45$ °C. It is important to note that this critical thickness is not universal; it depends sensitively on device geometry and characteristic dimensions.

Natural convection in a lateral diffusion system

For structures featuring lateral vapor escape [31–33], the air gap is directly exposed to the ambient environment, contrasting sharply with the enclosed nature of upward diffusion configurations. This exposure introduces complex coupling between internal natural convection within the gap and external convective losses to the surroundings. Consequently, characterizing the heat transfer in lateral diffusion systems remains challenging.

Existing studies often lack the necessary theoretical depth or transparency. For instance, Bian et al. [31] focused solely on experimental performance metrics without supporting theoretical or numerical analyzes. Similarly, subsequent modeling efforts [33,34] omitted critical thermal boundary conditions and geometric parameters, leaving the role of natural convection ambiguous. Among these, Zhang et al. [32] provided the most detailed analysis. However, their approach employed an oversimplified equivalent treatment: rather than resolving the coupled heat transfer from the emitter, across the air gap, to the water surface, they imposed an empirical heat flux boundary condition at the water surface, $q'' = h_{\mathrm{evap}}(T_w - T_a)$, where h_{evap} was derived from experimental data. Consequently, their work quantifies only the natural convection loss from the water surface to the ambient, without elucidating the internal convective effects within the air gap and external heat convection losses from the emitter.

Following the methodology outlined by Zhang et al. [32], natural convection losses from the water surface to the ambient are evaluated using the standard boundary-layer treatment for a horizontal plate. The Rayleigh number is evaluated at the water surface temperature T_w,

$$\mathrm{Ra} = \frac{g\beta_T (T_w - T_a) L_c^3}{\nu\alpha} \tag{14}$$

where L_c [m] is the characteristic length, taken as the length of the water surface, T_a [K] is the ambient temperature. This Rayleigh number determines the Nusselt number through an empirical correlation for laminar natural convection,

$$\mathrm{Nu} = f(\mathrm{Ra}, \mathrm{Pr}) \tag{15}$$

for which Zhang et al. [32] adopted $\mathrm{Nu} = 0.54\,\mathrm{Ra}^{1/4}$. The Nusselt number, in turn, determines the convective heat transfer coefficient and the associated surface heat loss:

$$h_w = \frac{k_{\mathrm{air}}}{L_c} \mathrm{Nu} \tag{16}$$

$$q_{\mathrm{w,conv}} = h_w A_w (T_w - T_a) \tag{17}$$

where h_w [W/(m^2 K)] is the convective heat transfer coefficient at the water surface, k_{air} [W/(m·K)] is the thermal conductivity of air, $q_{\mathrm{w,conv}}$ [W] is the convective heat loss from the water to the ambient air, and A_w [m^2] is the surface area of the water.

Extending this framework, the natural convection loss from the heated emitter to the ambient ($q_{\mathrm{conv,1}}$) can be estimated similarly by substituting T_w with T_{emt} and accordingly adjusting the characteristic area:

$$\mathrm{Ra} = \frac{g\beta_T (T_{\mathrm{emt}} - T_a) L_c^3}{\nu\alpha} \quad \rightarrow \quad h_{\mathrm{emt}} = \frac{k_{\mathrm{air}}}{L_c} f(\mathrm{Ra}, \mathrm{Pr}) \quad \rightarrow \quad q_{\mathrm{emt,conv}} = h_{\mathrm{emt}} A_{\mathrm{emt}} (T_{\mathrm{emt}} - T_a) \tag{18}$$

where h_{emt} [W/(m^2 K)] is the convective heat transfer coefficient at the emitter surface, L_c [m] is the characteristic length of the emitter, and A_{emt} [m^2] is the surface area of the emitter.

Regarding the internal heat convection within the air gap, we adopt the same assumption as we do for upward diffusion systems. Given the geometry, thermal stratification, and the evaluated internal Rayleigh number, the air gap is treated as a purely conductive medium, effectively neglecting internal convection.

2.2.3. Forced convection: a realistic extension in the lateral diffusion system

Although forced convection has not been explicitly considered in previous studies, its inclusion represents a realistic extension toward practical operating conditions for lateral diffusion systems. When natural wind is present in outdoor operating conditions, the flow regime is characterized by the Reynolds number (Re), which is used to distinguish between laminar and turbulent regimes:

$$\mathrm{Re} = \frac{U_m\ L_c}{\nu} \tag{19}$$

where U_m [m/s] is the mean wind speed, L_c [m] is the characteristic length of the water surface, and ν [m^2/s] is the kinematic viscosity of air.

The estimation of convective heat transfer coefficients h_{emt} and h_w [W/(m^2·K)] followed a procedure similar to that used for the natural convection regime, utilizing different Nusselt number correlations with the Reynolds and Prandtl numbers as inputs [26,35]:

$$\mathrm{Nu} = f(\mathrm{Re}, \mathrm{Pr}) \tag{20}$$

$$h_{\mathrm{emt}} = \frac{k_{\mathrm{air}}}{L_c} \mathrm{Nu_{emt}}, \quad h_w = \frac{k_{\mathrm{air}}}{L_c} \mathrm{Nu_w} \tag{21}$$

where $\mathrm{Nu_{emt}}$ and $\mathrm{Nu_w}$ are the Nusselt numbers for the emitter and the water surface.

Defining the bulk air temperature in the air gap as T_{air}, the convective heat transfer rates are expressed as follows:

$$q_{\mathrm{emt,conv}} = h_{\mathrm{emt}} A_{\mathrm{emt}} \left(T_{\mathrm{emt}} - T_{\mathrm{air}}\right) \tag{22}$$

$$q_{\mathrm{w,conv}} = h_w A_w \left(T_w - T_{\mathrm{air}}\right) \tag{23}$$

It is worth noting that under forced convection, the dominant heat transfer mechanism shifts from surface-to-ambient losses to convective exchange with the bulk airflow. In such scenarios, the direction of heat flow is governed by the temperature difference between the surfaces and the bulk air (T_{air}). If T_{air} lies between the emitter temperature T_{emt} and the water surface temperature T_w (i.e., $T_{\mathrm{emt}} > T_{\mathrm{air}} > T_w$), the convective heat loss from the water surface reverses sign ($q_{\mathrm{w,conv}} < 0$). This indicates a convective heat gain by the water surface: the emitter transfers energy to the bulk airflow, which subsequently delivers energy to the water surface. Consequently, forced convection can act as a thermal bridge, coupling the emitter and the water surface through the fluid medium.

2.3. Heat transfer at the water surface

2.3.1. Interfacial energy balance

Evaporation at the water-air interface introduces strong heat-mass transfer couplings, which are critical for closing the system-level energy and mass balance. The interfacial energy balance accounts for the input heat across the air gap, the conductive loss to the bulk water, and the latent heat consumption for phase change. The energy balance (as shown in Fig. 3e) at the water-air interface can be expressed as:

$$q_{\mathrm{w,in}} = q_{\mathrm{cond,loss}} + q_{\mathrm{evp}} \tag{24}$$

$$= k_{\mathrm{water}} A_w \frac{T_w - T_{\mathrm{bottom}}}{L_{\mathrm{water}}} + \dot{m} h_{\mathrm{fg}} \tag{25}$$

where $q_{\mathrm{w,in}}$ [W] denotes the total energy from the emitter to the water surface via radiation, conduction, and convection, $q_{\mathrm{cond,loss}}$ [W] is the conduction heat loss to bulk water, q_{evp} [W] is the latent heat, k_{water} [W/(m·K)] is the thermal conductivity of water, A_w [m^2] is the surface area of water, T_w and T_{bottom} [K] denote the surface temperature and bottom temperature of water, respectively; L_{water} [m] is the distance from interface to bulk water, $\dot{m}$ [kg/s] is the evaporation rate, and h_{fg} [J/kg] is the enthalpy of evaporation of water.

The evaporation rate $\dot{m}$ is governed by two resistances: vapor transport resistance in the air gap and interfacial kinetic resistance. As verified by Cooper et al. [20], the interfacial resistance is negligible compared to the air-gap diffusion resistance. Thus, only the vapor mass transport resistance in the air gap is considered in the following.

2.3.2. Mass transfer for different vapor transport configurations

Analogous to heat transfer, mass transfer occurs through two mechanisms: molecular diffusion, similar to heat conduction, and convection, akin to convective heat transfer.

Mass transfer for enclosed upward diffusion systems

For upward diffusion systems, the air gap is typically small and thermally stable, which suppresses convection. Consequently, vapor transport occurs primarily via molecular diffusion across the gap. The evaporation rate can be evaluated as:

$$\dot{m} = \frac{D_{\mathrm{wa}}}{d} A_w M_{\mathrm{H_2O}} \left(C_{\mathrm{sat,w}} - C_{\mathrm{emt}} \right) \tag{26}$$

where $M_{\mathrm{H_2O}}$ [kg/mol] is the molar mass of a water molecule, A_w [m^2] is the evaporation area of the water surface, $C_{\mathrm{sat,w}}$ [mol/m^3] is the molar concentration of saturated water vapor adjacent to the water surface, C_{emt} [mol/m^3] is the molar concentration of water vapor near the photothermal layer, D_{wa} [m^2/s] is the mass diffusivity of water vapor in air, and d [m] is the thickness of the air gap.

Notably, the above analysis focuses solely on vapor diffusion from the water surface to the photothermal layer; the subsequent diffusion from the photothermal layer to the ambient follows a lateral diffusion mechanism, as discussed in the next section.

Mass transfer for open lateral diffusion systems

In lateral diffusion systems, the mass transfer mechanism differs significantly from that in upward configurations. Since the photothermal emitter is typically hydrophobic and non-evaporative, there is only a single vapor source: the water surface. This simplifies the problem to the convective mass transfer of vapor from a horizontal plate (the water surface) to the ambient environment.

This process can be characterized using the heat-mass transfer analogy. Depending on the flow regime, the Nusselt number (Nu) is replaced by the Sherwood number (Sh), and the Prandtl number (Pr) is replaced by the Schmidt number (Sc):

$$\text{Natural convection: } \mathrm{Nu} = f(\mathrm{Ra}, \mathrm{Pr}) \leftrightarrow \mathrm{Sh} = f(\mathrm{Ra_m}, \mathrm{Sc}) \tag{27}$$

$$\text{Forced convection: } \mathrm{Nu} = f(\mathrm{Re}, \mathrm{Pr}) \leftrightarrow \mathrm{Sh} = f(\mathrm{Re}, \mathrm{Sc}) \tag{28}$$

$$\mathrm{Ra_m} = \frac{g\beta_{\mathrm{m}}(C_{\mathrm{sat,w}} - C_\infty)L_c{}^3}{\nu D}, \ \mathrm{Sc} = \nu / D \tag{29}$$

where Ra_m [-] is the mass transfer Rayleigh number, β_{m} [m^3/mol] is the concentration expansion coefficient, L_c [m] is the characteristic length of the water surface, ν [m^2/s] is the kinematic viscosity of air, and D_{wa} [m^2/s] is the mass diffusivity of water vapor in air.

The evaporation rate $\dot{m}$ is calculated as follows:

$$\dot{m} = h_m A_w M_{\mathrm{H_2O}} \left(C_{\mathrm{sat,w}} - C_\infty \right) \tag{30}$$

$$h_m = \mathrm{Sh} D_{va} / L_c \tag{31}$$

where h_m [m/s] is the convective mass transfer coefficient.

3. Modeling approaches for contactless evaporation

Multiphysics modeling and simulation are essential tools for studying these systems. Existing studies adopt a variety of numerical approaches, each balancing model accuracy, implementation complexity, and computational efficiency differently. This section reviews the commonly used modeling and simulation approaches for contactless evaporation.

3.1. 1D modeling and simulation methods

One-dimensional (1D) modeling and simulation methods typically involve reasonable geometric and physical simplifications of complex systems, reducing multidimensional problems to one-dimensional governing equations along the dominant direction for the solution. The core advantages of these methods lie in their high computational efficiency, clear physical mechanisms, and the ability to rapidly conduct parametric studies and design iterations. They are particularly suitable for mechanistic exploration, system-level performance evaluation, and preliminary design optimization. Their primary implementation approaches include numerical solutions based on MATLAB programming and system modeling based on Simulink.

In numerical methods based on MATLAB, researchers directly solve the governing equations through self-programming, offering high flexibility. For instance, Zheng et al. [28] established a theoretical framework based on thermal and mass transport resistance networks to conduct a mechanistic study on a three-dimensional contactless solar evaporator. They utilized MATLAB's "fsolve" function to numerically solve the nonlinear coupled equations describing the process, aiming to calculate the theoretical evaporation rate and analyze the influence of different design parameters.

System modeling based on Simulink, on the other hand, intuitively constructs models through graphical and modular approaches. Its built-in powerful solvers facilitate the handling of dynamic and nonlinear problems, making it suitable for system-level transient performance analysis. For example, Cooper et al. [20] constructed a quasi-one-dimensional transient coupled heat and mass transfer model within the Simulink environment based on an equivalent thermal resistance network and custom physics modules. They solved it using the ode23t solver to gain a deeper understanding and prediction of the device's thermal performance under transient and nonlinear effects, particularly focusing on the evaporation and vapor superheating processes.

Overall, the fidelity of these simulation methods is highly dependent on the simplifying assumptions made by the modeler. While they face challenges when dealing with complex geometries and strongly nonlinear coupled problems, their efficiency and flexibility render them valuable tools in the early stages of theoretical research and engineering design.

3.2. 2D/3D modeling via finite element analysis

COMSOL Multiphysics is a powerful finite element analysis (FEA) platform renowned for its ability to handle coupled multiphysics problems seamlessly. Currently, most researchers use COMSOL for simulation, typically focusing on resolving the detailed spatial distribution of evaporation processes (e.g., temperature distribution, vapor concentration) under various conditions to gain a deeper understanding of the underlying physical mechanisms.

Table 2
Summary of FEA-based modeling and simulation approaches for contactless evaporation.

Ref.	Model dimension & Analysis type	Key physics fields	Primary simulation focus
[32]	3D, transient state	Transport of dilute species, Laminar flow, Heat transfer	Observe the distribution of salinity and temperature in the confined aquifer. Evaluate salt accumulation and heat loss under different design parameters.
[27]	3D, steady state	Moisture transport in air, Laminar flow, Heat transfer	Investigate the effects of key structural parameters (aperture area ratio, pore size, and air layer thickness) on heat and mass transfer, and determine the optimal values.
[34]	2D, steady state	Heat transfer	Observe water temperature distribution to demonstrate the effectiveness of photoelectric synergistic solid slippery surface (PESSS).
[36]	3D, transient state	Heat transfer	Verify, quantify, and visualize the thermal localization effect of sun umbrella to guide design and optimization.
[29]	2D, steady state	Moisture transport in air Heat Transfer	Demonstrate the porous structures can promote vertical water vapor transport and increase the moisture concentration within the condenser.
[37]	3D, steady state	Flow in porous media Heat transfer	Provide a theoretical basis and visual explanation for experimental design and performance optimization of contactless-interfacial (C-IF) evaporator.
[33]	3D, steady state	Moisture transport in air Heat transfer, Rarefied mass transport in porous media	Provide a theoretical basis and visual explanation for the experiment
[38]	3D symmetry, N/A	Moisture transport in air Flow in porous media Heat transfer	Provides theoretical model support for experiments. Comprehensively evaluates the evaporation performance of the apparatus.

The choice between 2D and 3D modeling in finite element analysis represents a fundamental trade-off between computational efficiency and physical fidelity. 2D models typically simplify the geometry by assuming symmetry or representing a cross-section, thereby significantly reducing the mesh element count and computational time. This approach is advantageous for parametric studies, preliminary design exploration, and understanding the core physics in a simplified domain. However, 2D models inherently neglect three-dimensional effects, such as edge effects, non-uniform flows, or complex geometric features that are not axisymmetric. Conversely, 3D models provide a complete and physically accurate representation of the system, capturing all spatial phenomena and complex geometries. This comes at the cost of substantially higher computational resources and longer solution times, often limiting the scope of parametric sweeps or requiring high-performance computing for transient analyzes. Therefore, 2D simulations are often employed for conceptual verification and rapid performance trend analysis, while 3D simulations are crucial for validating final designs, quantifying absolute performance metrics, and investigating systems where three-dimensional transport is dominant.

Based on this methodological distinction, the existing literature utilizing COMSOL for contactless evaporation can be categorized, as summarized in Table 2. The table covers model dimensions, analysis types, key coupled physics fields, and the primary research focus of each study.

From the modeling perspective presented in Table 2, simulations range from steady-state to transient analyzes, and from simplified studies of 2D cross-sections to complex 3D geometries. The coupled key physical fields generally include heat transfer, laminar or porous media flow, and are often combined with dilute species transport or moisture transport in air. The main objectives of the simulations focus on visualization and quantitative analysis, such as observing the distribution of temperature, salinity, or humidity within the system, and exploring the impact of key structural parameters (such as air gap thickness) on heat and mass transfer, thereby providing a theoretical basis for experimental design and guiding performance optimization.

4. Innovative designs of contactless evaporators

In recent years, numerous innovative designs of contactless evaporators have emerged, which can be summarized into three main research directions: the development of novel evaporator materials, the optimization of evaporator geometry, and the integration of contactless and conventional interfacial evaporation. Most studies address two or three of these aspects simultaneously. These strategies have driven substantial improvements in evaporation efficiency and system stability, which are systematically described in the following sections.

4.1. Development of novel absorber and emitter materials

In contactless evaporation, the efficient conversion of solar irradiance into infrared radiation is crucial for the evaporation process. Since this conversion primarily depends on the material properties of the photothermal layer (the absorber and emitter), research on photothermal layers holds a central position in this field. Table 3 presents detailed information about the photothermal layer materials in different studies, arranged chronologically.

According to Table 3, the main research trends in photothermal layer materials can be summarized. Regarding the absorber, it typically employs high-absorptance coatings, such as commercial selective coatings [20,27,28,31,36], special black paints [32,33], or nanomaterials (e.g., graphene) [34,39–44], while the radiation-emitting layer predominantly uses high-emittance industrial black paints [20,27,28,31–33,36,39–42]. In recent years, integrated designs utilizing the same material for both sunlight absorption and longwave emission have emerged [34,37,43,44]. Concerning substrate materials, early studies primarily adopted high conductivity materials such as aluminum plates [20,28,31–33,36]. This has since expanded to include copper [27,29], stainless steel [39–42], carbon fiber fabrics [34], and flexible composite materials [37,38,43].

In terms of performance, under one sun without electrical augmentation, operating temperatures mostly fall between 60 °C and 90 °C,

Table 3
Properties and thermal performance of photothermal layer materials in current studies.

Ref. (year)	Absorber material	Absorptance	Emitter material	Emittance	Substrate material	Operation temperature
[20] (2018)	Alanod eta plus commercial coating	0.924	Zynolyte Hi-Temp high-temperature black paint	0.941	Aluminum plate	N/A
[36] (2020)	Selective solar absorption coating	0.95	High-infrared-emissivity black industrial furnace paint	0.94	Aluminum plate	70 ± 2 °C under 1 sun
[31] (2021)	TiNOX commercial coating	0.92	4SD Hi-Temp Paint (black high-temperature paint)	0.947	Aluminum plate	88 °C under 1 sun
[32] (2022)	Rust-Oleum 245198 black paint	0.953	Same as absorber	N/A	Aluminum plate	60 °C under 1 sun
[39–42] (2022 & 2023)	Cr-Fe-Mn nanoporous composite oxide layer	0.90	Rust-Oleum flat black protective enamel	0.94	SS202 stainless steel perforated plate	73-85 °C at peak
[27] (2023)	Selective absorption coating	0.9632	Zynolyte Hi-Temp Paint (black paint)	0.7820	Copper plate	N/A
[33] (2023)	Black paint coating	0.931	Same as absorber	N/A	Aluminum	81 °C under 1 sun
[43] (2024)	Solar-reduced graphene oxide (SRGO)	> 0.95	Same as absorber	N/A	Carbon fiber fabric	86.9 °C under 1 sun + 2.5 V
[34] (2024)	Nanographite and Carbon nanotube mixture	> 0.8045	Nanographite coating	N/A	High-oxygen silicon fiber cloth composite	150 °C under 1 sun + 1.25 V
[38] (2024)	Carbon black particles (embedded in hydrogel)	0.97	PVDF film with microsphere array	0.94	Transparent hydrogel matrix and hydrophilic fiber cloth	33.1 °C under 1 sun
[44] (2024)	Crystalline nanocellulose (CNC) composite film	N/A	Same as absorber	N/A	Glass Petri dish	63.8 °C under 250 W lamp with 15 cm distance
[28] (2024)	Linuo-Paradigma solar selective absorption layer	0.93	AERVOE Zynolyte Hi-Temp Paint	0.92	Aluminum plate	60.37 °C under 1 sun with 1 mm air gap
[29] (2025)	CuO conversion	0.928	Multi-walled Carbon Nanotubes (MWCNTs) coating	0.885	Copper foam	61.5 °C under 1 sun
[37] (2026)	Traditional Chinese ink coating	0.8828	Same as absorber	N/A	Flower of woody plants	N/A

with electrically or structurally augmented designs reaching higher values and secondary-stage configurations reaching lower values. Overall, the research trend in this field is advancing toward the application of nanocomposite materials, the development of flexible/non-metallic substrates, and the pursuit of multifunctional integration.

4.2. Geometric design and vapor transport optimization

The geometric configuration of a contactless evaporator governs two quantities that together determine evaporation performance: the radiative heat flux delivered to the water surface and the rate at which the generated vapor can be removed from the water surface. Because these two quantities are coupled through the geometry of the emitter plate and the air gap, geometric optimization is central to advancing contactless evaporation beyond its current efficiency limitations. Research to date can be organized into two categories: designs that retain the parallel emitter-water configuration established by Cooper et al. [20] while modifying the emitter plate and surrounding components (Fig. 4), and designs that depart from the parallel constraint altogether by reconfiguring the overall device geometry (Fig. 5).

4.2.1. Geometry optimization within the parallel configuration

In the original design by Cooper et al. [20] (Fig. 4a), the emitter and water reservoir are arranged as parallel flat plates separated by an air gap. This configuration maximizes the radiative view factor F_{12} between the two surfaces, which approaches unity when the plate separation is small relative to the plate dimensions. However, a solid, continuous emitter plate also acts as a physical barrier to vapor escape: water vapor generated at the liquid surface must diffuse laterally to the edges of the device before reaching the ambient environment. As the device area increases, the lateral diffusion path lengthens, creating a vapor transport bottleneck that suppresses the local vapor concentration gradient driving evaporation. This bottleneck becomes the dominant performance limitation for any contactless evaporator intended for practical, larger-than-laboratory scales.

The most widely explored strategy to alleviate this bottleneck is the introduction of openings in the emitter plate to provide vertical vapor escape pathways. Several distinct approaches have been investigated. Zhang et al. [32] investigated the role of pores in the thermal insulation foam surrounding the emitter rather than in the emitter plate itself (Fig. 4b). By varying the size and number of pores in polystyrene foam, they demonstrated that appropriately sized openings allow vapor to escape vertically without significantly degrading thermal insulation. They used 3D transient COMSOL simulations to visualize the resulting salinity and temperature distributions within the confined water layer.

Regarding the involvement of the perforated emitter, Zheng et al. [27] conducted a systematic parametric study of hole diameter, hole spacing (pitch), and air layer thickness using 3D steady-state COMSOL simulations coupled with moisture transport modeling (Fig. 4c). They identified optimal values for the aperture area ratio and pore size that balance vapor permeability with radiative area loss. Mohiuddin et al. [42] fabricated a Cr-Fe-Mn nanostructure absorber on a perforated stainless steel plate and experimentally studied the effect of air gap distance on evaporation performance (Fig. 4d), finding that performance is sensitive to the gap thickness but did not provide a theoretical model to predict the optimum. Menon et al. [36] used a perforated

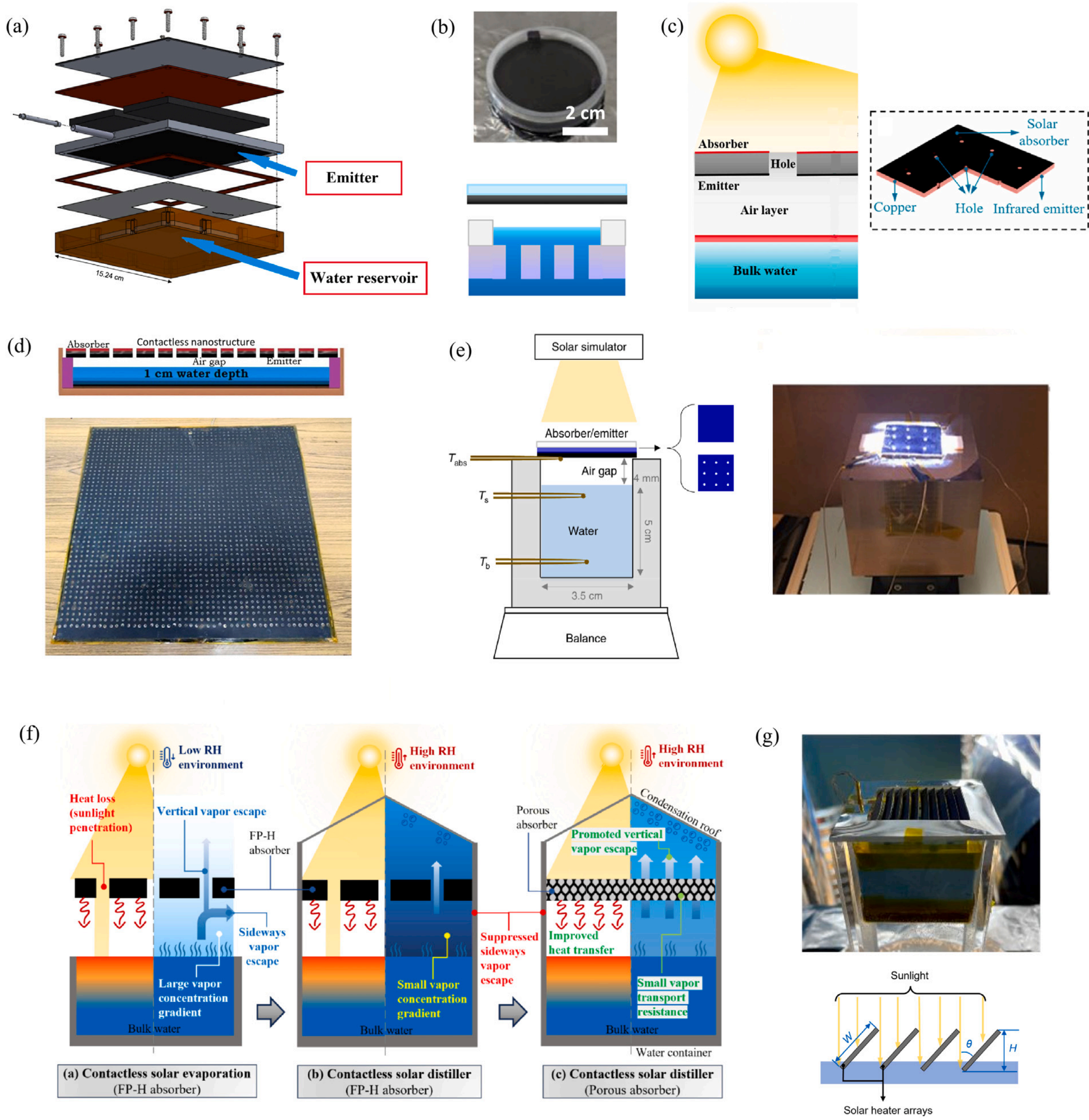

Fig. 4. Geometry optimization of the evaporator in the parallel configuration. (a) Parallel structure proposed by Cooper et al. [20], with the emitter and water reservoir arranged in parallel [20]. (b) Effect of pore size and number in the thermal insulation foam; the upper image is the fabricated device and the lower image is the schematic illustration [32]. (c) Zheng et al. [27], (d) Mohiuddin et al. [42] and (e) Menon et al. [36]: hole structure in the photothermal layer that enhance water vapor permeability. (f) Comparison of porous structures for photothermal layers: the left and middle panels show perforated metal plates, and the right shows a porous metal structure [29]. (g) The photothermal layer cut into several pieces and installed at a tilt angle, which preserves the total irradiated area while enhancing water vapor permeability [28]. All figures are adapted and reproduced with permission.

aluminum absorber in their photothermal umbrella design (Fig. 4e), demonstrating enhanced evaporation for wastewater management and validating the thermal localization effect through 3D transient COMSOL modeling.

Zheng et al. [29] advanced this line of investigation by directly comparing two fundamentally different porous architectures: perforated metal plates (with discrete circular holes in a solid sheet) and porous metal structures (copper foam with interconnected open-cell porosity), as shown in Fig. 4f. Their results demonstrated that the porous copper foam structure outperformed the perforated plates, achieving a higher water yield in a contactless solar distiller configuration. The authors attributed this to the interconnected pore network of the foam, which promotes vertical vapor transport more effectively than discrete holes while simultaneously providing improved sideways heat transfer. Importantly, the porous structure also increased the moisture concentration within the condenser, as confirmed by 2D steady-state COMSOL moisture transport simulations. However, the study did not quantify the reduction in the radiative view factor F_{12} caused by the foam structure relative to a solid plate or a perforated plate with equivalent open area, leaving the radiative penalty of porosity uncharacterized.

An alternative strategy that avoids perforating the emitter was proposed by Zheng et al. [28]. Rather than introducing holes, they cut the emitter plate into several smaller pieces and installed them at a tilt angle relative to the horizontal (Fig. 4g). This arrangement preserves the total solar-irradiated area (and therefore the total absorbed solar power) while creating angled channels between adjacent

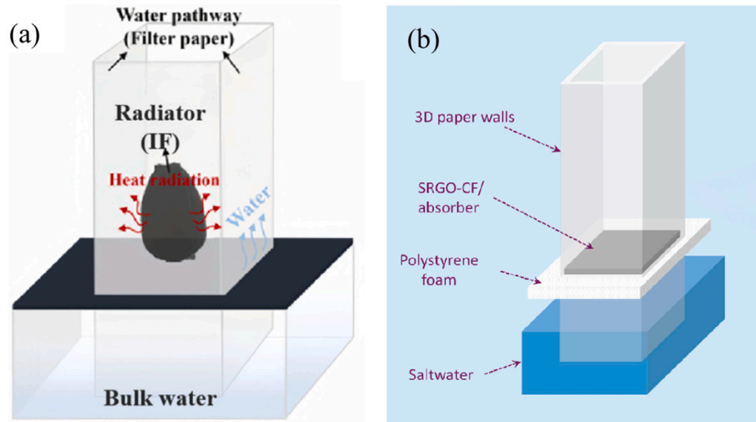

Fig. 5. Designs beyond the parallel configuration. In both (a) Su et al. [37] and (b) Wilson et al. [43], the evaporation surface is extended perpendicular to the horizontal water surface, forming four evaporation surfaces. Figures are adapted and reproduced with permission.

plate segments through which vapor can escape vertically. Using a MATLAB-based thermal and mass resistance network model, they analyzed the influence of tilt angle and channel dimensions on evaporation rate, demonstrating that this 3D configuration achieves both high performance and scalability. Their model also revealed the conduction-to-radiation flux crossover at approximately 4 mm air gap thickness, a finding with implications for all parallel-configuration designs.

4.2.2. Designs beyond the parallel configuration

A separate line of research has explored device geometries that abandon the parallel emitter-water arrangement entirely. The motivation is to increase the total evaporation surface area beyond the projected footprint of the solar absorber, thereby extracting more evaporative output per unit of collected solar energy.

Su et al. [37] developed a water-heat separation evaporator that extends the water evaporation surface vertically, forming four evaporation surfaces perpendicular to the horizontal water reservoir (Fig. 5a). In this configuration, the emitter radiates not only downward to the horizontal water surface but also laterally to the vertical water films. The design exploits a thermal radiation-convection hybrid mechanism: infrared radiation from the emitter heats the water surfaces, while the buoyancy-driven convection of warm, humid air within the enclosed structure further assists vapor transport. 3D steady-state COMSOL simulations of flow in porous media and heat transfer were used to provide a theoretical basis for the design and to visualize the temperature and flow fields.

Wilson et al. [43] adopted a similar strategy using solar-reduced graphene oxide (SRGO) deposited on carbon fiber fabric as the absorber-emitter, with 3D paper walls extending the evaporation surface vertically (Fig. 5b). Combined with electrothermal augmentation (2.5 V), the device achieved all-day operation with anti-salt-fouling properties. The vertical evaporation surfaces increase the total evaporation area, while the SRGO carbon fiber provides a flexible, non-metallic alternative to the rigid aluminum plates used in most parallel designs.

These non-parallel designs represent an important conceptual departure from the Cooper et al. [20] baseline. By decoupling the evaporation area from the solar energy collection area, they relax the constraint that the evaporation rate is bounded by the solar flux intercepted per unit of horizontal area. Consequently, the rates reported for these designs (5.06 and 2.78 $kg/m^2/h$ under one sun) are normalized to the projected solar footprint rather than to the larger actual evaporating surface, and they exceed the single-sun limit for a horizontal surface, which is 1.4 $kg/m^2/h$ [37]. The surplus is supplied by sensible heat drawn from the surrounding air across the extended vertical films, which Su et al. [37] quantified through an energy-balance analysis and attributed to the environmental energy harvested by the three-dimensional structure. However, this advantage comes with added geometric complexity, and the radiative view factors between the emitter and the multiple water surfaces become more difficult to calculate and optimize. Furthermore, both designs inherently combine contactless and interfacial evaporation mechanisms (the vertical water films receive heat from both radiation from the emitter and conduction from the wetted structure), placing them at the intersect between the purely contactless paradigm and the hybrid systems discussed in Section 4.3.

4.3. Hybrid designs combining contactless and interfacial evaporation

The preceding sections have established that contactless evaporation offers complete salt-fouling immunity at the cost of lower efficiency compared to contact-based interfacial evaporation. Interfacial evaporation, conversely, achieves high solar-to-vapor conversion by placing the photothermal material in direct contact with a thin water film; however, this contact inevitably leads to salt accumulation under high-salinity conditions [12,13]. A natural question arises: can the two approaches be combined within a single device to capture the advantages of both?

Several recent studies have explored this hybrid strategy, and their designs can be organized based on which evaporation mode serves as the primary driver and which serves a supporting role.

4.3.1. Interfacial evaporation as a thermal insulation layer for contactless heating

In a standard contactless evaporator, the infrared radiation > 1.4 μm emitted by the photothermal layer is absorbed within the top 1 cm of the water body (Fig. 2). However, the bulk water beneath this thin heated layer acts as a large thermal reservoir. Heat conducted downward from the surface into the bulk water represents a significant energy loss that does not contribute to evaporation. This loss is inherent to any design in which the water reservoir is deep relative to the infrared penetration depth.

Wang et al. [33] addressed this problem by introducing a capillary-driven interfacial evaporation layer between the emitter and the bulk water reservoir (Fig. 6a). In their solar-thermo-radiative evaporator, a spectrum-selective absorber converts broadband sunlight into infrared radiation, which heats a thin water film transported to the evaporation surface by capillary threads. The capillary transport layer serves a dual function: it supplies water to the evaporation interface while simultaneously acting as a thermal barrier that limits heat conduction into the bulk water below. Salt crystallizes at the edges of the capillary structure through marginal crystallization, enabling continuous operation with simultaneous vapor generation and salt harvesting. The

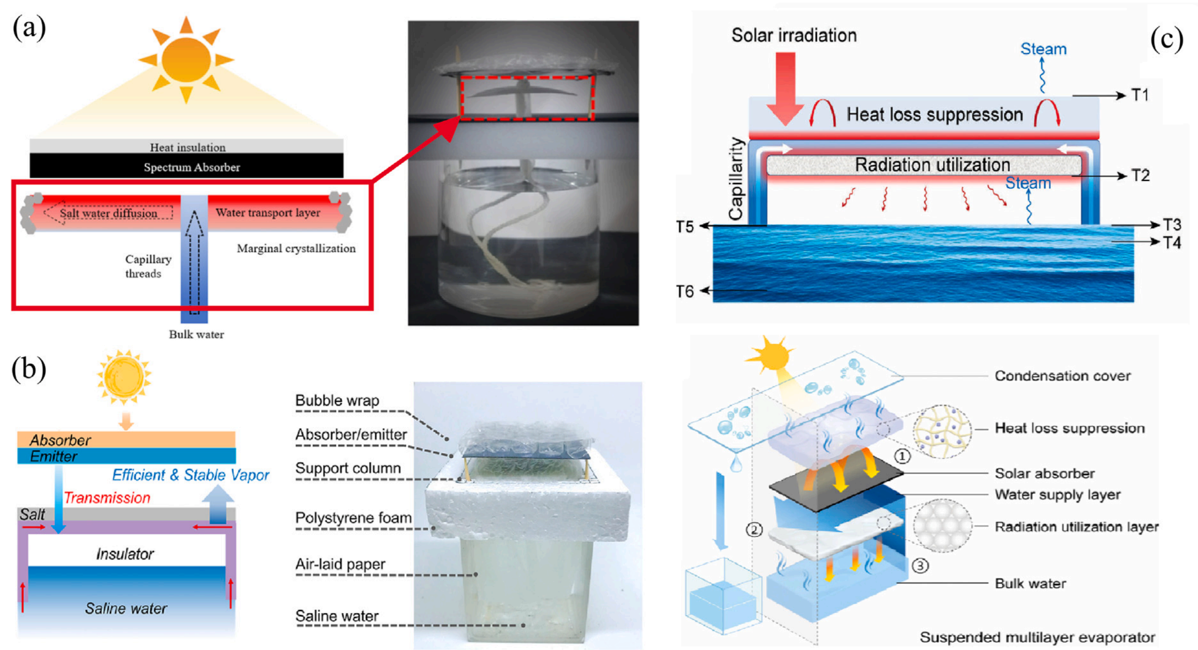

Fig. 6. Designs combining contactless and interfacial evaporation. In (a) Wang et al. [33] and (b) Bian et al. [31], interfacial evaporation is used to further reduce heat conduction loss to the bulk water. (c) Design that recovers residual heat from interfacial evaporation through a contactless stage [38]. All figures are adapted and reproduced with permission.

device was modeled using 3D steady-state COMSOL simulations that couple moisture transport, heat transfer, and rarefied mass transport in porous media.

Bian et al. [31] adopted a similar architecture with different materials (Fig. 6b). Their design uses a TiNOX absorber-emitter plate suspended above a polystyrene foam insulator, with an air-laid paper layer providing a capillary water supply from the saline water below. The air gap between the emitter and the insulator-paper assembly enables contactless radiative heating, while the capillary paper layer minimizes the water volume exposed to direct heating. The insulator physically interrupts the heat conduction pathway to the bulk water, and support columns provide structural stability without creating significant thermal bridges. The device achieved an absorber temperature of 88 °C under one sun, with stable vapor production.

In both designs, the capillary layer does not function as a conventional interfacial evaporator (where the photothermal material directly contacts bulk water). Instead, the thin capillary layer primarily acts as a water supply mechanism and a conductive heat loss barrier. The evaporation itself is still driven by contactless infrared radiation from the overhead emitter. This distinction is important because the hybrid architecture retains the salt-management advantage of contactless evaporation (salt crystallizes at the capillary edges, away from the absorber) while reducing the largest single energy loss in a purely contactless system (conduction to bulk water).

4.3.2. Contactless evaporation as a secondary stage for residual heat recovery

He et al. [38] proposed an inverted hybrid architecture in which interfacial evaporation is the primary mode of evaporation, and contactless evaporation serves as a secondary stage for heat recovery (Fig. 6c). In their suspended multilayer design, the upper layer is a conventional interfacial solar evaporator: a solar absorber with a capillary water supply that produces vapor directly. Below this primary evaporation stage, a radiation utilization layer captures the residual thermal energy that would otherwise be lost through the bottom of the interfacial evaporator. This layer consists of a PVDF film with a microsphere array (emittance of 0.94) that re-emits captured heat as infrared radiation across a second air gap to a lower water surface, driving a second contactless evaporation stage.

This architecture inverts the usual role assignment. Rather than using contactless evaporation as the primary mechanism, with interfacial evaporation providing thermal insulation (as in the Wang et al. [33] and Bian et al. [31] designs), it uses interfacial evaporation as the primary high-efficiency stage and contactless evaporation as a secondary energy recovery mechanism. The advantage is that the primary stage operates at the high efficiency typical of interfacial evaporation (because the absorber directly contacts a thin water film), while the secondary contactless stage extracts additional evaporation from energy that would otherwise be wasted. The reported water surface temperature in the contactless stage was only 33.1 °C under one sun, reflecting the limited thermal energy available after the primary interfacial stage has extracted the majority of the solar input. The device was characterized using 3D COMSOL simulations with symmetry boundary conditions, coupling moisture transport, porous media flow, and heat transfer.

5. Performance, durability, scalability, and cost characteristics of contactless evaporator designs

Existing contactless solar evaporator designs have progressed from proof-of-concept demonstrations toward increasingly application-oriented systems. In addition to enhancing vapor generation without direct absorber–brine contact, recent studies have expanded their focus to freshwater production, anti-scaling behavior, environmental tolerance, modular deployment, and economic feasibility. However, the practical relevance of these advances cannot be assessed from a single indicator alone. A meaningful evaluation requires the combined consideration of apparent performance, operational durability, environmental adaptability, scalability, and lifecycle cost.

5.1. Summary of performance metrics

Table 4 summarizes the representative apparent performance reported for existing contactless solar evaporation systems, including evaporation rate, freshwater productivity, efficiency or gained output ratio (GOR), along with the corresponding operating conditions and reported temperatures. Since most studies report multiple experimental cases under varying irradiation levels, feed waters, or structural parameters, we selected one representative dataset from each study. Priority was given to cases with the most complete set of monitored indicators; when completeness was equivalent, we selected the case with the highest target value while also considering the data that the authors emphasized in the abstract, introduction, or conclusions.

The values listed in Table 4 should be interpreted as apparent comparative indicators rather than strictly equivalent benchmarking results. Evaporation rate, freshwater productivity, efficiency, and GOR do not represent the same physical quantity, and their reported values are strongly affected by device geometry, feed water composition, illumination level, condensation pathway, etc.. In particular, some studies report total water evaporated, whereas others report only collected condensate. Accordingly, Table 4 is most useful for identifying broad performance trends and characteristic design advantages, rather than for direct one-to-one ranking across all devices.

Standalone contactless evaporators remain the dominant configuration in the literature. For parallel layouts, representative evaporation rates are generally below 1.1 kg/(m^2·h) under approximately one-sun illumination, with reported efficiencies typically ranging from 38.8% to 68.3% [20,28,32]. Some studies also report freshwater productivity rather than evaporation rate, as presented in Mohiuddin et al. [42] and Zheng et al. [29]. This distinction is important because vapor generation and collected freshwater output are not necessarily equivalent, especially when condensation efficiency becomes limiting.

By contrast, non-parallel configurations often exhibit much higher apparent evaporation rates. For example, Su et al. [37] and Wilson et al. [43] reported representative values of 5.06 and 2.78 kg/(m^2·h), respectively, suggesting that geometric reconfiguration can substantially enhance local heat confinement and vapor transport. Hybrid systems demonstrate similarly high performance. While Wang et al. [33] and Bian et al. [31] reported representative evaporation rates of only 0.633 and 0.67 kg/(m^2·h), He et al. [38] achieved 2.83 kg/(m^2·h) under one-sun illumination, indicating the performance gain that can arise from multistage transport or heat-recycling strategies. Notably, some hybrid devices achieve relatively high apparent evaporation rates even at modest reported temperatures, implying that temperature alone is not a sufficient descriptor of device performance across different architectures.

Overall, current contactless systems span a wide performance window, from below 1 to above 5 kg/(m^2·h) under nominal one-sun conditions. This diversity reflects the strong dependence of reported performance on structure, transport pathway, and metric definition. However, comparison remains constrained by inconsistent reporting standards, incomplete condensate data, and insufficient clarification of experimental boundaries in some studies. Future work should therefore move toward harmonized reporting of evaporation rates, collected freshwater productivity, efficiency or GOR, operating conditions, and clearly defined temperature measurement positions.

5.2. Durability, operational reliability, and environmental adaptability

Beyond performance metrics, the practical value of a contactless evaporator depends on whether stable operation can be maintained during prolonged use and under variable environmental conditions. Representative information is summarized in Table 5. Compared with interfacial evaporators, contactless architectures are intrinsically attractive because the photothermal component is physically separated from the bulk saline feed, which can suppress direct salt deposition on the absorber and reduce irreversible performance deterioration.

Anti-scaling behavior is therefore one of the most consistent advantages reported in the literature. Early work by Cooper et al. [20] established the basic rationale of sustaining evaporation without direct absorber fouling, and later studies further localized salt crystallization onto low-cost or replaceable transport media rather than the active photothermal component [37,43]. Related designs also reported stable operation with minimized salt accumulation at the evaporation interface [28,29]. These findings indicate that durability in contactless systems is governed not only by material selection but also by the geometric regulation of heat, water, and crystallization pathways.

Operational reliability may likewise benefit from the passive nature of many current designs. Because pumps, valves, fans, or active control modules are often unnecessary, mechanically induced failure modes can be reduced, which is advantageous for off-grid or decentralized deployment [29,36]. Some studies further suggest that optimized three-dimensional or modular architectures can preserve stable heat and mass transfer during prolonged operation [28]. Environmental adaptability has also been partially demonstrated, for example, through operation with non-ideal saline sources [42], large open configurations [36], and modular deployment concepts intended for villages, islands, or coastal regions [29].

Nevertheless, the information base for durability and adaptability remains incomplete. In many cases, stability is demonstrated only through short cyclic laboratory tests using simplified saline feed solutions. Long-term outdoor validation, multi-parameter environmental testing, and post-operation characterization of structural or interfacial degradation are still limited. In addition, operational reliability is often inferred from the retained evaporation rate alone, without a simultaneous assessment of condensate collection stability, structural integrity, or hydraulic transport consistency. Future studies should therefore adopt more rigorous durability protocols involving realistic feed water matrices, extended outdoor operation, and coupled monitoring of both vapor generation and freshwater recovery.

5.3. Scalability and cost analysis

Scalability and economic viability remain decisive constraints on practical deployment. Although many laboratory-scale devices exhibit high evaporation performance and strong anti-scaling behavior, these advantages do not automatically persist at larger scales. Scale-up may introduce altered heat and mass transfer pathways, weakened edge-effect control, structural integration challenges, and nonuniform operating conditions. At the same time, real-world competitiveness depends not only on material costs but also on fabrication simplicity, infrastructure demands, maintenance burdens, service lifetime, and ultimately, the levelized cost of water (LCOW). Representative information is summarized in Table 6.

Several studies suggest that structurally optimized contactless systems have favorable scale-up potential. Zheng et al. [28] reported only about a 3% reduction in evaporation rate after enlargement, indicating that a three-dimensional configuration can preserve similar heat and mass transfer pathways across scales. Menon et al. [36] validated a three-dimensional thermal model against laboratory and outdoor experiments and used it to predict pond-scale performance, showing that the enlarged convective space at large scales improves vapor transport rather than degrades it. In parallel, Zheng et al. [27] established a validated cross-scale heat and mass transfer model, highlighting the importance of eliminating sidewall heat losses and optimizing geometric parameters during scale-up. These studies collectively suggest that rational geometric redesign, rather than simple area replication, is central to successful engineering scale up.

From a manufacturing perspective, several contactless evaporator designs are attractive because they use widely available materials and simple fabrication routes [37,42,43]. Modular or array-expandable concepts have also been proposed for village- or island-scale desalination applications [29]. Similarly, He et al. [38] projected quantifiable energy-saving and energy-recovery benefits for large-scale deployments with evaporation footprints exceeding 100 m^2.

Current economic evidence is promising but heterogeneous. Very low material or unit investment costs have been reported in some

Table 4
Representative apparent performance of current contactless solar evaporation devices.

Reference	Evaporation rate [kg/(m^2 h)]	Freshwater productivity [kg/(m^2 h)]	Efficiency/GOR	Operating condition	Emitter/evaporation-surface temperature
Standalone contactless evaporation devices					
Parallel configuration					
Cooper et al. [20]	0.936	N/A	38.8%	1.5 sun; DI water	≈147 °C; 100 °C
Zhang et al. [32]	0.75	N/A	51%	1 sun; DI water	≈60 °C; ≈35 °C
Zheng et al. [27]	0.797	N/A	50.3%	1 sun; DI water	N/A
Mohiuddin et al. [42]	N/A	0.126	27.8%	734.46 W/m^2; nil salt lake water	87.5 °C; 61.1 °C
Menon et al. [36]	0.62	N/A	43%	1 sun; pure water	72 °C; ≈42 °C
Zheng et al. [29]	0.83	0.16	N/A	1 sun; DI water	61.5 °C; 45.6 °C
Zheng et al. [28]	1.03	N/A	68.3%	1 sun; DI water	N/A
Non-parallel configuration					
Su et al. [37]	5.06	N/A	N/A	1 sun; 3.5 wt% simulated seawater	53.8 °C; N/A
Wilson et al. [43]	2.78	N/A	84.5%	1 sun; pure water	62 °C; 22–23 °C
Hybrid evaporation-mechanism devices					
Wang et al. [33]	0.633	N/A	44%	1 sun; pure water	>80 °C; 40 °C
Bian et al. [31]	0.67	N/A	44%	1 sun; pure water	88 °C; 60.5 °C
He et al. [38]	2.83	N/A	N/A	1 sun; pure water	33.1 °C; 30 °C

Note: Values are representative *apparent* metrics extracted from the literature and are not strictly equivalent benchmarking data. Reported evaporation rate, freshwater productivity, efficiency, and GOR depend on device geometry, projected-area definition, feed water composition, irradiation level, condensation pathway, and thermal accounting boundary. For each study, the representative dataset was selected by prioritizing indicator completeness, then highest target performance, while also considering values emphasized by the authors.

Table 5
Representative evidence on durability, operational reliability, and environmental adaptability of current contactless solar evaporator designs.

Reference	Durability/anti-scaling evidence	Reliability evidence	Environmental adaptability evidence	Main limitation
Cooper et al. [20]	Direct absorber–brine contact avoided; original anti-scaling rationale established	Stable laboratory vapor generation demonstrated	No dedicated adaptability assessment	Early proof-of-concept only
Zhang et al. [32]	Floating confined-water-layer design suggests reduced salt accumulation	Passive self-floating operation	Potential for large-area floating deployment	Durability evidence mainly qualitative
Zheng et al. [27]	Anti-scaling implications inferred from transport modeling	No experimental reliability validation	No dedicated adaptability evaluation	Modeling-focused study
Mohiuddin et al. [42]	Reduced direct salt deposition on active absorber; 20-year service life proposed	Annual maintenance estimated at 15% of annual fixed cost	Demonstrated with nil salt lake water	Limited long-term fouling characterization
Menon et al. [36]	Contactless umbrella configuration avoids conventional direct-contact scaling	Fully passive operation favors off-grid reliability	Pond-scale feasibility supported by validated model; open convection space	Environmental robustness not systematically quantified
Zheng et al. [29]	Stable operation with minimized salt accumulation at photothermal surface	Passive, modular, unattended operation	Proposed for village/island deployment	Limited long-term field data
Zheng et al. [28]	Stable extended operation; reduced edge-effect-driven salt buildup	Cross-scale thermal/mass-transfer consistency	Potential beyond laboratory scale	Limited multi-environment validation
Su et al. [37]	Salt crystallization shifted away from main photothermal component	Simple structure; replaceable low-cost materials	No dedicated adaptability verification	Lacks engineering-scale validation
Wilson et al. [43]	Salt precipitated on auxiliary media rather than active absorber	Simple hybrid assembly; low-maintenance concept	No systematic outdoor assessment	Long-term structural stability unclear
Wang et al. [33]	No dedicated durability assessment	Reliability not systematically discussed	No explicit adaptability validation	Stability evidence insufficient
Bian et al. [31]	Peelable salt layer and reusable structure suggest improved fouling management	Reusable configuration implies basic operational stability	No dedicated multi-factor environmental testing	Evidence largely qualitative
He et al. [38]	Large-scale multilayer design suggests stable thermal operation	100 m^2 anticipated deployment scenario supports system-level reliability	Outdoor-oriented large-area applicability implied	Detailed anti-scaling/degradation analysis lacking

Note: Evidence differs substantially in depth and form. Some studies provide direct cyclic or operational observations, whereas others support durability or adaptability only indirectly through structural design or qualitative discussion. Long-term outdoor validation, multiparameter environmental testing, and post-operation characterization remain limited in most reports.

systems, including \$2.5–3.9/m^2 (U.S. dollar basis) for the self-floating confined-water-layer evaporator [32], \$8.27/m^2 for the STPV design [31], and \$1.31/m^2 for the suspended multilayer evaporator [38]. More complete lifecycle analysis was provided by Zheng et al. [28], who reported a capital cost of \$210.34/m^2, a total investment of \$259.76/m^2 including land, and an LCOW of \$0.87/ton (\$0.89/m^3) over a 25-year lifetime. At a smaller device scale, Mohiuddin et al. [42] estimated a manufacturing cost of \$135 per unit, a service life of 20 years, and a water cost of \$0.08/L. Although these metrics are not directly comparable due to different accounting boundaries,

Table 6
Representative evidence on scalability and economic performance of current contactless solar evaporator designs.

Reference	Scalability evidence	Cost indicator	Techno-economic implication	Main limitation
Cooper et al. [20]	No dedicated scale-up study	No cost analysis	Proof-of-concept only	No engineering/economic validation
Zhang et al. [32]	Floating configuration compatible with large-area deployment; no quantified retention data	Material cost: $2.5–3.9/m^2$	Very low raw-material cost	Limited scale-up evidence
Zheng et al. [27]	Validated cross-scale model; 125% baseline gain after removing sidewall loss; 473.3% gain after optimization	No quantified cost analysis	Guides rational scale-up design	No field-scale validation
Mohiuddin et al. [42]	Mature chemical oxidation route; compact structure; site adaptability	$135 per unit; $0.08/L; maintenance 15% of annual fixed cost; 20 yrs life	Potential for decentralized purification	Cost metric not directly comparable with LCOW
Menon et al. [36]	Pond-scale performance predicted by validated model; enlarged convection improved transport	No precise areal or lifecycle cost	Passive operation may reduce land and auxiliary-energy demand	Incomplete cost accounting
Zheng et al. [29]	Modular design expandable into large arrays	Qualitative low-cost assessment only	Low infrastructure and maintenance demand	Limited quantitative costing
Zheng et al. [28]	Only ~ 3% attenuation after scale-up; 3D structure mitigated edge effects	$210.34/m^2$ capital cost; $259.76/m^2$ total investment; LCOW $0.87/ton ($0.89/m^3$); $20.82/(m^2$ yrs) energy-saving benefit; 25 yrs life	Strong lifecycle competitiveness	Few directly comparable studies
Su et al. [37]	Commercial materials; simple processing; mass-production potential	No cost analysis	Low fabrication threshold	No engineering-scale validation
Wilson et al. [43]	Simple sunlight-reduction synthesis; scalable hybrid preparation	Qualitative low-cost assessment only	Lower fabrication and maintenance burden	Limited quantitative economics
Wang et al. [33]	No dedicated scale-up analysis	No cost analysis	Practical deployment potential unclear	Limited translational discussion
Bian et al. [31]	Qualitative scale-up potential only	Material cost: $8.27/m^2$	Biomass-compatible low-cost substrate	Mainly material-cost evidence
He et al. [38]	100 m^2 anticipated deployment scenario; 12.1 kW energy saving and 5.4 kW energy recuperation	Unit investment cost: $1.31/m^2$	Strong potential for large engineering systems	Limited long-term cost boundary details

Note: Economic boundaries vary substantially across studies. Reported values may refer to raw-material cost, unit manufacturing cost, capital investment, water cost, or lifecycle cost, and are therefore not directly comparable without normalization. Scalability evidence is likewise heterogeneous, ranging from simulation and laboratory enlargement to limited engineering demonstrations.

they collectively indicate that contactless systems can be economically attractive when passive operation, simple fabrication, and anti-scaling maintenance advantages are effectively integrated.

Overall, existing studies indicate meaningful promise in both scale-up potential and economic feasibility. However, the existing evidence is still insufficient for robust engineering or commercial assessment. Recent thermo-economic analyzes of solar still variants likewise suggest that commercialization remains limited by water cost, durability, and scale-dependent system integration, even when laboratory-scale productivity improvements are substantial [45,46]. Quantitative scale-up studies remain limited; economic metrics are reported with inconsistent boundaries, and broader system-level factors such as land use, installation logistics, and environmental externalities are rarely evaluated within a unified framework.

5.4. Comparison with traditional interfacial evaporation

Traditional solar interfacial evaporation and contactless evaporation represent two distinct technical paradigms for solar-driven desalination, exhibiting fundamental differences in heat transfer mechanisms, operational performance, structural design, and practical applicability (Table 7).

Conventional interfacial evaporation relies on direct thermal coupling between the photothermal layer and the surface water film or wetted substrate, establishing a low-thermal-resistance heat delivery pathway that enables efficient interfacial heat localization. This structural advantage endows traditional interfacial evaporation with superior single-stage apparent evaporation performance and relatively unobstructed vapor transport near the heating surface, making it inherently advantageous for achieving a high evaporation flux. However, its inherent structural feature of direct contact between the photothermal material and saline water leads to prominent salt fouling risks; continuous desalination of high-salinity water inevitably causes salt accumulation and scaling on the photothermal surface, severely restricting long-term operational durability unless elaborate auxiliary salt management strategies are implemented. Additionally, its thermal management primarily focuses on inhibiting conductive heat loss to bulk water while balancing water supply and salt back-diffusion, with mature, simple, and diverse structural architectures that facilitate practical deployment.

In contrast, contactless evaporation adopts a completely different heat delivery mode, where thermal energy is predominantly transferred across an air gap via longwave infrared radiation, supplemented by conductive and convective heat transfer depending on structural geometry. The physical separation of the photothermal emitter from the brine fundamentally eliminates direct salt deposition on the photothermal surface, delivering an intrinsic anti-fouling capability and exceptional long-term operational stability under high-salinity conditions, which is the core competitive advantage of this technology. Nevertheless, the introduced air gap creates additional thermal resistance and vapor transport resistance, resulting in lower single-stage evaporation performance compared with traditional interfacial evaporation in standalone working configurations. Vapor removal further becomes a critical performance bottleneck, especially in enclosed or parallel structural designs. In terms of system design and thermal regulation, contactless evaporation poses more complex optimization challenges, requiring coordinated tuning of multiple parameters, including emitter optical and thermal properties, the radiative view factor, air-gap thickness, vapor permeability, and convective heat loss.

Table 7
Qualitative comparison between traditional solar interfacial evaporation and contactless evaporation for desalination.

Aspect	Traditional interfacial evaporation	Contactless evaporation
Heat-delivery pathway	Direct thermal coupling between the photothermal layer and the thin water film or wetted substrate	Thermal energy delivered across an air gap primarily by longwave infrared radiation, with possible conductive/convective contributions depending on geometry
Salt fouling tendency	Direct salt accumulation on the photothermal surface is a major risk during prolonged desalination of saline feedwater	Direct salt deposition on the photothermal layer is fundamentally suppressed because the photothermal surface is physically separated from brine
Single-stage apparent evaporation performance	Generally higher because of lower thermal resistance and efficient interfacial heat localization	Often lower in standalone configurations because the air gap introduces additional heat-transfer and vapor-transport resistance
Vapor-transport limitation	Usually less restricted near the heating surface, although water supply and salt back-diffusion remain important	Vapor removal can become a major bottleneck, especially in enclosed or parallel configurations
Thermal management challenge	Suppressing conductive heat loss to bulk water while maintaining water supply and salt management	Balancing radiative view factor, air-gap thickness, vapor permeability, and convective heat loss
Structural/design complexity	Mature and diverse architectures; generally simpler thermal pathway	Requires coupled optimization of emitter properties, view factor, insulation, vapor escape pathways, and geometry
Long-term durability under high salinity	Can be limited by scaling unless special salt-management strategies are introduced	Intrinsically favorable for anti-scaling and potentially more stable under prolonged saline operation
Best-fit application logic	More suitable when maximizing evaporation flux is the primary target	More suitable when anti-fouling stability, passive operation, and desalination durability are prioritized

Overall, the two evaporation technologies exhibit complementary application characteristics: traditional interfacial evaporation is optimal for scenarios prioritizing maximum evaporation flux, while contactless evaporation is more suitable for desalination systems that emphasize long-term stability, passive operation, and excellent anti-scaling performance in high-salinity environments.

6. Current limitations in contactless evaporator designs

The preceding sections show that contactless evaporation has developed rapidly in terms of physical understanding, material selection, structural innovation, and application-oriented evaluation. At the same time, several recurring limitations also emerge from the current literature. These limitations are not confined to a single study or device type; rather, they reflect broader unresolved issues that cut across the fundamental, modeling, design, and validation levels of the field. Based on the evidence reviewed above, current limitations can be summarized into four main aspects.

6.1. Mechanistic and modeling limitations

As discussed in the sections on fundamental principles and modeling approaches, the current understanding of contactless evaporation is still uneven across different transport processes and device configurations. For enclosed upward-diffusion systems, the physical picture is relatively clear: radiative transfer, conductive heat transport across the air gap, and diffusion-limited vapor transport can all be described within a reasonably consistent framework. By contrast, lateral-diffusion and more open configurations remain less rigorously resolved. In these systems, the coupling among internal transport in the air gap, external natural or forced convection, and vapor removal to the ambient is considerably more complex; yet, it is often simplified or only partially treated in existing analyzes.

This uneven mechanistic treatment is reflected in the current modeling literature. Most numerical studies focus on specific temperature, salinity, or humidity distributions within a chosen geometry, but many remain strongly dependent on simplifying assumptions, incomplete boundary conditions, or partial coupling of the relevant physics fields. In particular, transient environmental effects, external wind interaction, and coupled condensation behavior are still rarely incorporated. In addition, although radiative heating is the defining feature of contactless evaporation, most current analyzes treat thermal radiation in a broadband manner. The spectral dependence of emitter–water coupling, which is directly relevant to the physical basis of the technology, has not yet been systematically integrated into mainstream design models.

6.2. Material limitations in the photothermal layer

The review of absorber and emitter materials shows that current contactless evaporators have achieved considerable practical simplicity by relying on commercially available selective coatings, black paints, metallic plates, and, more recently, flexible or nanocomposite substrates. However, this material development pathway also reveals a clear limitation: in most existing systems, the absorber and emitter are still designed primarily for high overall solar absorption and high overall infrared emission, rather than for finely tuned spectral matching between solar harvesting, thermal infrared emission, and water absorption characteristics.

This limitation is important because contactless evaporation fundamentally depends on radiative heat delivery across an air gap. Even though many studies report acceptable apparent evaporation performance using broadband emitters, the material layer is still rarely optimized as a spectrally engineered radiative interface. Moreover, several recent designs adopt the same material for both absorber and emitter functions, which simplifies fabrication but may constrain the independent optimization of solar absorptance and infrared emittance. The current literature also provides only limited comparative evidence regarding the long-term durability, manufacturability, and cost-performance trade-offs of more advanced nanostructured or flexible materials. As a result, material innovation in this field has expanded faster than the establishment of clear material-selection criteria for practical desalination systems.

6.3. Geometric and architectural design limitations

The sections on geometric optimization and hybrid designs indicate that structural innovation has been the most active driver of recent progress. Parallel configurations, perforated emitters, porous structures, tilted segmented emitters, non-parallel architectures, and hybrid systems that combine contactless and interfacial evaporation have all been proposed to alleviate the intrinsic bottlenecks of vapor escape, thermal confinement, and conductive heat loss. However, these developments also make clear that the field still lacks a unified design framework capable of comparing competing architectures on a common mechanistic basis.

A particularly important unresolved issue is the trade-off between radiative delivery and vapor transport. Openings or porous pathways can facilitate vapor escape, but they may also reduce the effective radiative area, alter view factors, and complicate heat transfer pathways. Although several studies have examined individual geometric parameters, most do so through case-specific parameter sweeps rather than through coupled optimization across the full design space. Consequently, current device geometries remain largely heuristic, and it is still difficult to determine whether reported gains arise mainly from better vapor transport, stronger environmental energy uptake, altered normalization area, or genuinely more efficient internal heat management.

The same limitation extends to hybrid and non-parallel systems. These architectures demonstrate that contactless evaporation can be combined productively with interfacial evaporation or expanded evaporation surfaces, but they also blur the boundary between purely contactless and mixed-mechanism operation. In some cases, relatively high apparent evaporation rates are achieved by increasing the effective evaporation area beyond the projected solar footprint or by drawing sensible heat from the environment. Such strategies are scientifically valuable, but they complicate direct comparison with conventional parallel contactless systems and make performance attribution less straightforward. In addition, current hybrid systems remain mostly single-stage in their thermal utilization, with little evidence of systematic latent-heat recovery through staged condensation–evaporation integration.

6.4. Application-oriented validation limitations

The application-oriented assessment presented in the previous section further shows that the validation of current contactless evaporators remains incomplete. Reported performance spans a wide range, but the meaning of this variation is often difficult to interpret because evaporation rate, freshwater productivity, efficiency, and gained output ratio (GOR) are not reported consistently across studies. Wang et al. [47] have argued that for practical solar desalination, the GOR, defined as the ratio of the latent heat of collected freshwater to the total energy input, is a more meaningful performance metric than the evaporation rate or solar-to-vapor conversion efficiency. Moreover, in many cases, apparent evaporation performance is emphasized, whereas condensate collection performance is absent or only partially characterized. This is a major limitation for desalination-oriented evaluation because vapor generation alone does not establish practical freshwater output.

The same problem appears in durability, scalability, and cost assessment. Although anti-scaling behavior is one of the most consistent advantages reported for contactless architectures, the supporting evidence is often limited to short laboratory tests with simplified saline feeds. Long-term outdoor operation, realistic fouling matrices, structural degradation analysis, and maintenance-oriented performance tracking are still uncommon. Similarly, several studies discuss favorable scale-up potential or low material costs, but quantitative large-module demonstrations and harmonized life-cycle cost boundaries remain limited. Economic indicators such as raw-material cost, unit investment, and levelized cost of water are reported using different accounting frameworks, which makes robust comparison difficult. Therefore, while the field has clearly advanced beyond proof-of-concept, its application readiness is still constrained by insufficiently standardized and insufficiently realistic validation.

7. Future research priorities for contactless evaporation

The limitations identified above indicate that future progress in contactless evaporation will depend not only on proposing new device structures but also on strengthening mechanistic rigor, material selectivity, architectural integration, and application-oriented validation. Accordingly, future research priorities can be organized along the same four dimensions.

7.1. Mechanism-resolved modeling and environmental transport analysis

A first priority is to establish more comprehensive mechanistic models that cover the full range of relevant transport regimes. Future studies should move beyond the current emphasis on enclosed, quasi-one-dimensional, or steady-state cases and give greater attention to lateral-diffusion, open, and environmentally exposed configurations in which internal transport, ambient convection, and vapor removal are strongly coupled. A more rigorous treatment of these systems would improve the understanding of how geometry-dependent boundary conditions shape real evaporation behavior.

Model development should also better integrate the transport processes that are currently treated separately. In particular, radiative heat transfer, conduction or convection across the air gap, vapor diffusion, and condensation should be incorporated within unified frameworks wherever possible. This does not necessarily require every study to adopt a fully high-order simulation approach, but it does require clearer physical boundaries, stronger experimental validation, and more transparent justification of simplifying assumptions. Such efforts would help distinguish which observed performance gains arise from fundamental architectural improvements and which depend mainly on case-specific conditions.

In addition, future modeling should progressively incorporate spectral and environmental realism. Because contactless evaporation is defined by radiative coupling across an air gap, it would be especially valuable to integrate wavelength-dependent emitter behavior, water absorption, and outdoor influences such as wind, humidity, and diurnal variation. This would provide a stronger mechanistic bridge between controlled laboratory analysis and practical operating conditions.

7.2. Spectrally informed material design and practical material selection

A second priority is to shift material development from predominantly broadband photothermal design toward more spectrally informed absorber–emitter engineering. The literature already shows that commercially available coatings and black emitters can support effective contactless evaporation, but future performance gains may increasingly depend on how well the photothermal layer is tailored to the distinct spectral roles of solar absorption and infrared emission. More explicit attention should therefore be given to the spectral matching among absorber properties, emitter properties, and the wavelength-dependent absorption characteristics of water.

This priority also implies that absorber and emitter functions should not always be treated as interchangeable. Integrated single-material designs may remain attractive for simplicity and cost reduction, but comparative research is needed to determine when such simplification is advantageous and when separate optimization of solar absorptance and thermal emittance is more beneficial. Material studies should therefore move beyond reporting only overall absorptance, emittance, and apparent evaporation performance; they should instead clarify how the choice of material influences the entire radiative heat-delivery pathway.

At the same time, practical selection criteria should be strengthened. Future work should evaluate advanced materials not only by laboratory performance but also by long-term stability, manufacturability, substrate compatibility, cost, and environmental robustness. Such comparative assessment would help define whether emerging nanostructured, flexible, or multifunctional materials offer meaningful practical advantages over simpler industrial coatings in desalination-oriented deployment.

7.3. Coupled geometric optimization and deeper system integration

A third priority is to establish a more unified design framework for geometry and system architecture. Future studies should treat the radiative view factor, vapor permeability, conductive leakage, and effective evaporation area as coupled design variables rather than as isolated structural features. This is especially important for perforated, porous, segmented, and non-parallel emitters, where apparent performance improvements often arise from several interacting mechanisms at once. More systematic optimization across these coupled variables would make it easier to identify genuinely advantageous architectures and compare them on a common basis.

This effort should also extend to hybrid systems. Existing hybrid designs already show that different evaporation modes can complement one another, particularly when interfacial components are used to suppress conductive heat loss or when contactless stages recover residual heat. However, future research should move beyond simple mode combinations and explore how heat, vapor, and salt-management functions can be deliberately distributed across different parts of an integrated device. In this sense, architectural design should be guided less by adding features incrementally and more by assigning each component a clear thermodynamic role.

A particularly important direction is the deeper integration of contactless evaporation into staged or heat-recovery-based desalination systems [48,49]. Because current hybrid devices remain largely single-stage in their thermal utilization, the potential of contactless architectures for multistage condensation–evaporation coupling remains largely unexplored. Increased attention to staged heat recovery could help advance the field from single-pass vapor generation toward more desalination-relevant system efficiency.

7.4. Standardized desalination-oriented validation and field relevance

A fourth and particularly urgent priority is to establish a more unified experimental and reporting framework for contactless desalination systems. As discussed in the preceding section, the existing literature remains difficult to compare because evaporation rate, collected freshwater productivity, efficiency, and GOR are reported inconsistently and are often derived under different optical, thermal, and hydraulic boundaries. For this reason, standardized testing should be treated not as a secondary methodological issue but as a prerequisite for meaningful progress assessment across the field.

At the laboratory level, future studies should adopt a clearer minimum reporting protocol anchored in unified testing standards to ensure data comparability. The framework proposed by Li et al. [50] offers a readily implementable solution. At a minimum, desalination-oriented experiments should report the illumination source and calibrated irradiance, spectral characteristics if non-standard light is used, ambient temperature and relative humidity, feed water composition, projected-area definition, test duration, dark evaporation correction method, and the spatial positions of temperature measurements. For electrically assisted Joule heat-based systems, the electrical energy input should be reported explicitly and included in the overall energy accounting. In addition, studies involving condensation should report both the evaporation rate and the collected freshwater productivity under the same operating conditions so that the gap between vapor generation and actual freshwater recovery can be evaluated directly.

Within this framework, GOR should be given greater emphasis as a core desalination metric [47]. The evaporation rate remains useful for mechanistic comparison, but it is insufficient on its own for evaluating practical water production, especially in enclosed systems where condensation efficiency may become the dominant limitation. Future contactless desalination studies should therefore move toward coordinated reporting of at least three linked indicators: evaporation rate, collected freshwater productivity, and GOR. Such a reporting structure would make it possible to distinguish whether performance gains arise from better evaporation, better condensation, or improved overall thermal utilization. Furthermore, reaching meaningful GOR values will require integrating high-efficiency condensation modules, such as forced-convection and radiative-cooling condensers, rather than relying on passive solar distillation alone [51].

7.5. Build a prioritized research roadmap

A staged research roadmap may help implement this transition more effectively. In the near term, priority should be placed on protocol harmonization and comprehensive data reporting so that representative devices can be compared on a more consistent basis. In the medium term, benchmark testing of several standard contactless configurations under matched conditions would help validate theoretical models and identify the most reliable design variables. Over the longer term, standardized outdoor testing and techno-economic assessments should be incorporated, including performance under variable solar irradiance, wind, humidity, and realistic saline feeds.

When measurable targets are desirable, they are best framed as indicative milestones rather than rigid universal thresholds. For example, near-term studies should aim to report complete evaporation–collection–GOR datasets rather than evaporation rate alone; closed desalination systems should increasingly quantify the freshwater collection ratio, $\dot{m}_{\mathrm{coll}}/\dot{m}_{\mathrm{evap}}$, under matched operating conditions; and larger-scale demonstrations should move toward reporting levelized water cost using clearly defined accounting boundaries. Likewise, durability assessments would be more informative if they extended beyond short cyclic tests to prolonged operation, with explicit reporting of evaporation and/or condensation rate degradation, salt accumulation locations, and maintenance requirements. These measurable milestones would provide a more practical roadmap for field maturation while remaining flexible enough to accommodate the diversity of existing contactless designs.

8. Conclusions

This review has systematically examined contactless evaporation as a distinct solar-desalination architecture in which the photothermal layer is physically separated from saline water, and heat is delivered to the evaporation interface primarily through longwave infrared radiation across an air gap. This configuration fundamentally avoids direct salt deposition on the photothermal surface and, therefore, offers a clear anti-fouling advantage over conventional interfacial evaporation.

The current knowledge base shows that contactless evaporation is governed by coupled radiative, conductive, convective, and vapor-transport processes. For enclosed upward-diffusion systems, the dominant mechanisms can be described within a relatively clear framework of radiative heating, conductive transport across the air gap, and diffusion-limited vapor removal. For lateral-diffusion and more open systems, however, the coupling among internal transport, ambient convection, and vapor removal is considerably more complex and remains insufficiently resolved. Correspondingly, existing modeling approaches, ranging from 1D reduced-order analysis to 2D/3D finite-element simulation, have provided valuable mechanistic insight, but they still fall short of fully capturing spectral effects, transient outdoor conditions, and system-level freshwater recovery.

Recent progress in the field has primarily followed three directions: the development of absorber–emitter materials, the geometric optimization of the evaporator, and hybridization with conventional interfacial evaporation. Material studies have expanded from commercial selective coatings and industrial black paints to nanocomposites, flexible substrates, and integrated photothermal layers. Geometric innovation has moved from the original parallel configuration toward perforated, porous, segmented, tilted, and non-parallel architectures designed to relieve vapor-transport limitations while maintaining radiative heat delivery. Hybrid systems have further shown that contactless and interfacial evaporation can be combined to suppress conductive heat loss or recover residual heat.

Despite these advances, several limitations remain. First, the mechanistic understanding of open and lateral-diffusion systems is still incomplete, especially under realistic environmental conditions. Second, most current devices rely on broadband absorber and emitter designs, with limited spectral optimization of emitter–water radiative coupling. Third, a fundamental trade-off persists between vapor permeability and radiative delivery in porous or perforated structures. Fourth, application-oriented evaluation remains fragmented because the evaporation rate, freshwater productivity, efficiency, and gained output ratio are reported inconsistently, while long-term outdoor validation and harmonized techno-economic assessments are still limited.

Overall, contactless evaporation should not be viewed simply as a lower-efficiency variant of interfacial evaporation but as a complementary desalination pathway with distinct physical logic and practical value. Its main strength lies in combining passive operation with intrinsic resistance to salt fouling, making it particularly attractive for stable solar desalination under high-salinity conditions. Future progress should therefore focus on mechanism-resolved modeling, spectrally informed material design, coupled geometric optimization, multistage heat-recovery integration, and standardized desalination-oriented testing based on evaporation rate, collected freshwater productivity, and GOR. Advancing along these directions will be essential for translating contactless evaporation from laboratory-scale demonstrations into practically relevant solar freshwater production systems.

CRediT authorship contribution statement

Zhiheng Qiu: Writing – original draft. **Xin Wei:** Writing – review & editing. **Yinghao Song:** Writing – review & editing. **Nan Deng:** Writing – original draft. **Ronghui Qi:** Writing – review & editing. **Omar AlAli:** Writing – review & editing, Project administration. **Mengying Li:** Writing – review & editing, Supervision, Project administration, Funding acquisition.

Declaration of Generative AI and AI-assisted technologies in the writing process

During the preparation of this work, the authors used GPT-5 to improve language and readability. After using this tool, the authors reviewed and edited the content as needed and took full responsibility for the content of the publication.

Declaration of competing interest

The authors declare that they have no known competing financial interests or personal relationships that could have appeared to influence the work reported in this paper.

Acknowledgments

The authors gratefully acknowledge the substantial support from the Hong Kong University Grants Committee (UGC) under project number C6003-22Y, as well as the support from The Hong Kong Polytechnic University under project number P0055995.

Data availability

Data will be made available on request.

References

[1] P.H. Gleick, Water in Crisis, Oxford University Press, New York, 1993.
[2] United Nations Educational, Scientific and Cultural Organization (UNESCO), The united nations world water development report 2024: water for prosperity and peace, 2024, URL: https://digitallibrary.un.org/record/4042870?v=pdf.
[3] S. Honarparvar, X. Zhang, T. Chen, A. Alborzi, K. Afroz, D. Reible, Frontiers of membrane desalination processes for brackish water treatment: A review, Membranes 11 (4) (2021) 246.
[4] N. Ghaffour, T.M. Missimer, G.L. Amy, Technical review and evaluation of the economics of water desalination: Current and future challenges for better water supply sustainability, Desalination 309 (2013) 197–207.
[5] M. Elimelech, W.A. Phillip, The future of seawater desalination: energy, technology, and the environment, Science 333 (6043) (2011) 712–717.
[6] H. Sharon, K. Reddy, A review of solar energy driven desalination technologies, Renew. Sustain. Energy Rev. 41 (2015) 1080–1118.
[7] B.W. Tleimat, E.D. Howe, Comparative productivity of distillation and reverse osmosis desalination using energy from solar ponds, J. Sol. Energy Eng. (ISSN: 0199-6231) 104 (4) (1982) 299–304.
[8] X. Ibarra-Herrera, Solar multistage flash evaporation (smsf) as a solar energy application on desalination processes, Desalination 30 (1) (1979) 91.
[9] M. Telkes, Fresh water from sea water by solar distillation, Ind. Eng. Chem. 45 (5) (1953) 1108–1114.
[10] P. Hogan, A. Fane, G. Morrison, et al., Desalination by solar heated membrane distillation, Desalination 81 (1–3) (1991) 81–90.
[11] H. Ghasemi, G. Ni, A.M. Marconnet, J. Loomis, S. Yerci, N. Miljkovic, G. Chen, Solar steam generation by heat localization, Nat. Commun. 5 (1) (2014) 4449.
[12] R. Gu, Z. Yu, Y. Sun, P. Xie, Y. Li, S. Cheng, Enhancing stability of interfacial solar evaporator in high-salinity solutions by managing salt precipitation with janus-based directional salt transfer structure, Desalination 524 (2022) 115470.
[13] Y. Fan, et al., Enhanced solar-to-heat efficiency of photothermal materials containing an additional light-reflection layer for solar-driven interfacial water evaporation, ACS Appl. Energy Mater. 4 (3) (2021) 2932–2943.
[14] M. Morciano, M. Fasano, S.V. Boriskina, E. Chiavazzo, P. Asinari, Solar passive distiller with high productivity and marangoni effect-driven salt rejection, Energy & Environ. Sci. 13 (10) (2020) 3646–3655.
[15] Y. Wang, X. Sun, S. Tao, Rational 3D coiled morphology for efficient solar-driven desalination, Environ. Sci. Technol. 54 (24) (2020) 16240–16248.
[16] N. Xu, H. Zhang, Z. Lin, J. Li, G. Liu, X. Li, W. Zhao, X. Min, P. Yao, L. Zhou, et al., A scalable fish-school inspired self-assembled particle system for solar-powered water-solute separation, Natl. Sci. Rev. 8 (10) (2021) nwab065.
[17] H. Shan, Z. Ye, J. Yu, R. Wang, Z. Xu, Improving solar water harvesting via airflow restructuring using 3D vapor generator, Device 1 (4) (2023).
[18] R. Zhu, K. Li, D. Wang, J. Fei, J.Y. Tan, S. Li, J. Zhang, H. Li, S. Fu, Biomimetic optimized concept with murray networks for accelerated solar-driven water evaporation, Chem. Eng. J. 467 (2023) 143383.
[19] Z. Liu, Z. Zhou, N. Wu, R. Zhang, B. Zhu, H. Jin, Y. Zhang, M. Zhu, Z. Chen, Hierarchical photothermal fabrics with low evaporation enthalpy as heliotropic evaporators for efficient, continuous, salt-free desalination, ACS Nano 15 (8) (2021) 13007–13018.
[20] T.A. Cooper, et al., Contactless steam generation and superheating under one sun illumination, Nat. Commun. 9 (1) (2018) 5086.
[21] N. Deng, P. Dong, Z. Wang, M. Li, Quantifying the effects of spectral and directional distribution of radiation on its propagation in saline water, Appl. Therm. Eng. 258 (2025) 124536.
[22] Y. Song, S. Fang, N. Xu, J. Zhu, Solar-driven interfacial evaporation technologies for food, energy and water, Nat. Rev. Clean Technol. 1 (1) (2025) 55–74.
[23] H. Bai, T. Zhao, M. Cao, Interfacial solar evaporation for water production: from structure design to reliable performance, Mol. Syst. Des. Eng. 5 (2) (2020) 419–432.
[24] L. Hou, S. Li, Y. Qi, J. Liu, Z. Cui, X. Liu, Y. Zhang, N. Wang, Y. Zhao, Advancing efficiency in solar-driven interfacial evaporation: strategies and applications, ACS Nano 19 (10) (2025) 9636–9683.
[25] S.-L. Wu, H. Chen, H.-L. Wang, X. Chen, H.-C. Yang, S.B. Darling, Solar-driven evaporators for water treatment: challenges and opportunities, Environ. Sci.: Water Res. Technol. 7 (1) (2021) 24–39.
[26] J.P. Holman, Heat Transfer: Tenth Edition, McGraw-Hill Education, 2010.
[27] S. Zheng, J. Yu, Z. Xu, Modeling and analysis of contactless solar evaporation for scalable application, Appl. Sci. 13 (6) (2023) 4052.
[28] S. Zheng, J. Yu, H. Shan, J. Gao, R. Wang, Z. Xu, High-performance and scalable contactless solar evaporation with 3D structure, Sci. Bull. (2024).
[29] S. Zheng, J. Yu, R. Li, B. Zhou, Z. Xu, Contactless solar distiller with enhanced water yield via porous absorber, Desalination (2025) 119683.
[30] Y.A. Cengel, M.A. Boles, Thermodynamics: an engineering approach, Sea 1000 (8862) (2002) 287–293.
[31] Y. Bian, et al., Sustainable solar evaporation while salt accumulation, ACS Appl. Mater. & Interfaces 13 (4) (2021) 4935–4942.
[32] L. Zhang, et al., Highly efficient and salt rejecting solar evaporation via a wick-free confined water layer, Nat. Commun. 13 (1) (2022) 849.
[33] L. Wang, Y. Feng, Q. Liu, G. Liu, Solar-thermo-radiative evaporator for continuous steam generation and salt harvesting, Sol. Energy 250 (2023) 347–354.
[34] P. Guo, R. Jin, Z. Teng, K. Liu, L. Jiang, L. Heng, Photoelectric synergy solid slippery surface for all-day contactless evaporation, Chem. Eng. J. 497 (2024) 154784.
[35] Y.A. Çengel, A.J. Ghajar, Heat and Mass Transfer: Fundamentals & Applications, McGraw Hill LLC, 2025.
[36] A.K. Menon, I. Haechler, S. Kaur, S. Lubner, R.S. Prasher, Enhanced solar evaporation using a photo-thermal umbrella for wastewater management, Nat. Sustain. 3 (2) (2020) 144–151.
[37] J. Su, W. Du, Y. Xie, X. Lin, C. Shi, X. Dong, Y. Xu, J. Shi, C. Wang, Water-heat separation evaporator design for efficient solar steam generation utilizing thermal radiation-convection hybrid mechanism, Desalination (ISSN: 0011-9164) 618 (2026) 119455.
[38] N. He, X. Sun, H. Wang, B. Wang, D. Tang, L. Li, Dual-interface solar evaporator with highly-efficient thermal regulation via suspended multilayer design, Small 20 (38) (2024) 2402863.

[39] S. Afzal Mohiuddin, A. Kumar Kaviti, S. Rao Atchuta, S. Sakthivel, T. Harish, K. Vinay Kumar, T. Srinivasa Rao, A. Thaker, K. Vishwanath Reddy, A. Mohit Naga Sai, S. Ram Akkala, Performance analysis of non-contact nanostructure solar desalination system by varying water depth at a constant air gap, Sol. Energy (ISSN: 0038-092X) 247 (2022) 485–498.
[40] S.A. Mohiuddin, A.K. Kaviti, T.S. Rao, S. Sakthivel, Effect of water depth in productivity enhancement of fouling-free non-contact nanostructure desalination system, Sustain. Energy Technol. Assessments 54 (2022) 102848.
[41] S.A. Mohiuddin, A.K. Kaviti, T.S. Rao, S. Sakthivel, Performance analysis of a contactless nanostructure in solar-powered desalination system, Environ. Sci. Pollut. Res. 30 (6) (2023) 16277–16288.
[42] S.A. Mohiuddin, A.K. Kaviti, T.S. Rao, S. Atchuta, Effect of air gap in novel fouling-free non-contact nanostructure solar still for potable water application from lake water, J. Clean. Prod. 381 (2022) 135100.
[43] H.M. Wilson, T.A. Want, S.J. Lee, All-day, all-weather desalination using a contactless evaporator with antisalt fouling property, ACS Appl. Mater. & Interfaces 16 (50) (2024) 69450–69458.
[44] V. Kumar, A. Chandel, P. Upadhyay, S. Chakma, Enhanced total contact-less photothermal desalination by translucent thin film coating of crystalline nanocellulose, Langmuir 40 (24) (2024) 12343–12352.
[45] M. Elashmawy, A. Nafey, S.W. Sharshir, G.B. Abdelaziz, M.M. Ahmed, Experimental investigation of developed tubular solar still using multi-evaporator design, J. Clean. Prod. 443 (2024) 141040.
[46] A.A. Al-Nagdy, M. Omara, S.A. Sobhy, G.B. Abdelaziz, 4E assessment of pyramid distiller performance utilizing V-corrugated wick material and TiO2 nanoparticles with hybrid solar heating, Sol. Energy 278 (2024) 112796.
[47] Z. Wang, T. Horseman, A.P. Straub, N.Y. Yip, D. Li, M. Elimelech, S. Lin, Pathways and challenges for efficient solar-thermal desalination, Sci. Adv. 5 (7) (2019) eaax0763.
[48] E. Chiavazzo, M. Morciano, F. Viglino, M. Fasano, P. Asinari, Passive solar high-yield seawater desalination by modular and low-cost distillation, Nat. Sustain. 1 (2018) 763–772.
[49] Z. Xu, L. Zhang, L. Zhao, B. Li, B. Bhatia, C. Wang, K.L. Wilke, Y. Tu, J. Song, E.N. Wang, Extreme salt-resisting multistage solar distillation with thermohaline convection, Joule 7 (11) (2023) 2532–2551.
[50] X. Li, G. Ni, T. Cooper, N. Xu, J. Li, L. Zhou, X. Hu, B. Zhu, P. Yao, J. Zhu, Measuring conversion efficiency of solar vapor generation, Joule 3 (8) (2019) 1798–1803.
[51] I. Haechler, H. Park, et al., Exploiting radiative cooling for uninterrupted 24-hour water harvesting from the atmosphere, Sci. Adv. 7 (2021) eabf3978.